iScience

CellPress
OPEN ACCESS

Article

Single-nucleus transcriptomics reveal cardiac cell type-specific diversification in metabolic disease transgenic pigs

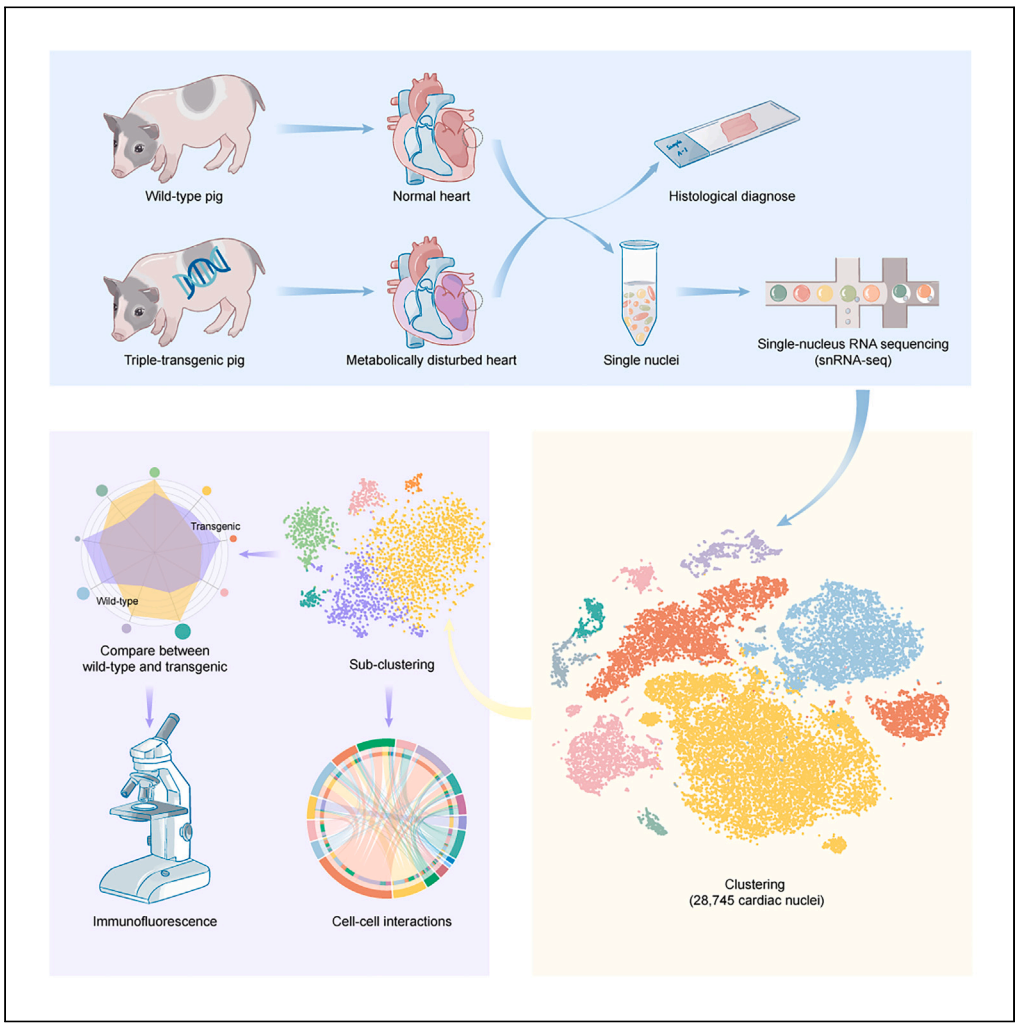

Jiakun Miao, Kaiyi Zhang, Yu Yang, ..., Cong Tao, Yanfang Wang, Shulin Yang

wangyanfang@caas.cn (Y.W.)
yangshulin@caas.cn (S.Y.)

Highlights

Metabolic disease-induced cardiac injury is characterized by mitochondrial damage

A single-cell atlas of healthy and metabolic-impaired porcine cardiac tissue

Metabolic disorders alter cardiac cellular composition, expression and interactions

Proinflammatory EC activation and reparative MAC depletion may lead to cardiac injury

Miao et al., iScience 27, 110015
June 21, 2024
https://doi.org/10.1016/j.isci.2024.110015

iScience

CellPress
OPEN ACCESS

Article

Single-nucleus transcriptomics reveal cardiac cell type-specific diversification in metabolic disease transgenic pigs

Jiakun Miao,[1] Kaiyi Zhang,[1] Yu Yang,[1] Shuang Xu,[1] Juan Du,[1] Tianwen Wu,[1] Cong Tao,[1] Yanfang Wang,[1,*] and Shulin Yang[1,2,*]

SUMMARY

Cardiac damage is widely present in patients with metabolic diseases, but the exact pathophysiological mechanisms involved remain unclear. The porcine heart is an ideal material for cardiovascular research due to its similarities to the human heart. This study evaluated pathological features and performed single-nucleus RNA sequencing (snRNA-seq) on myocardial samples from both wild-type and metabolic disease-susceptible transgenic pigs (previously established). We found that transgenic pigs exhibited lipid metabolism disturbances and myocardial injury after a high-fat high-sucrose diet intervention. snRNA-seq reveals the cellular landscape of healthy and metabolically disturbed pig hearts and identifies the major cardiac cell populations affected by metabolic diseases. Within metabolic disorder hearts, metabolically active cardiomyocytes exhibited impaired function and reduced abundance. Moreover, massive numbers of reparative LYVE1^{+} macrophages were lost. Additionally, proinflammatory endothelial cells were activated with high expression of multiple proinflammatory cytokines. Our findings provide insights into the cellular mechanisms of metabolic disease-induced myocardial injury.

INTRODUCTION

Obesity and related metabolic diseases, including metabolic syndrome (MetS) and type 2 diabetes mellitus (T2DM), are risk factors for cardiovascular diseases (CVDs) comprising coronary artery disease (CAD), myocardial disease, and heart failure (HF), resulting in increased mortality.[1-3] However, the mechanisms by which metabolic diseases trigger cardiac injury remain unknown due to the complexity of pathophysiology and the limited availability of human cardiac samples from patients with early-stage metabolic diseases.

The mammalian heart is composed of heterogeneous cell populations, and the delicate orchestration of these diverse cell types ensures the integrity of cardiac tissue anatomically and functionally.[4,5] During disease progression, heterogeneous cell populations generate specific responses. Thus, the identification of cell-specific disease-associated programs may provide necessary insights and opportunities for the treatment of diseases. Over the past decade, the rapid development of single-cell RNA sequencing (scRNA-seq) technology has made it possible to understand the mammalian heart (mainly in humans and mice) and reveal cellular expression pattern shifts in disease at the single-cell level.[6-9] Recent studies have revealed the importance of several cardiac cell types in cardiovascular events. For example, in HF patients, phenotypic remodeling of endothelial cells (ECs) affects the biological behavior of macrophages (MACs) and fibroblasts (FBs), thereby promoting cardiac inflammation and fibrosis.[10] In dilated cardiomyopathy (DCM) patients, FB activation and tissue-resident cardiac macrophage (RCM) depletion are major factors.[11] Although extensive work via scRNA-seq has been performed in humans for various cardiac diseases, research on metabolic disease-induced cardiac dysfunction is still lacking.

In contrast to rodent models, which exhibit significantly different cardiac physiology from that of humans, pigs are more similar to humans in terms of cardiovascular anatomy and cardiac physiology. Thus, they could serve as an ideal animal model for CVD research.[12] In our previous study, we successfully constructed a triple-transgenic (*PNPLA3*^{I148M}-*GIPR*^{dn}-*hIAPP*) pig model (TG pig) via the CRISPR-Cas9 technique. This model exhibited metabolic disorders (such as glucose intolerance and adipose tissue inflammation) after short-term high-fat high-sucrose diet (HFHSD) intervention,[13] thus providing promising evidence for the study of metabolic imbalance-related diseases. Herein, we fed TG pigs and wild-type (WT) pigs a long-term HFHSD (12 months), and lipid metabolism disorders, myocardial tissue edema, and mitochondrial damage were observed in TG pigs. We further performed single-nucleus RNA sequencing (snRNA-seq) on myocardium samples from both WT and TG pigs. We identified ten major cardiac cell types, described their intercluster and intracluster heterogeneity, revealed changes in the cellular composition and cell type-specific transcriptional patterns of cardiac tissue in metabolic diseases, and characterized

[1]State Key Laboratory of Animal Biotech Breeding, Institute of Animal Science, Chinese Academy of Agricultural Sciences (CAAS), Beijing 100193, China
[2]Lead contact
*Correspondence: wangyanfang@caas.cn (Y.W.), yangshulin@caas.cn (S.Y.)
https://doi.org/10.1016/j.isci.2024.110015

their cell type-specific diversification features and possible interactions. Our data provide a reference for the feasibility of clinical research on pig models and broaden insights for the specific treatment of metabolic disease-induced cardiac injury.

RESULTS

Systemic characteristics, cardiac function and pathological features of TG pigs

To evaluate the metabolic shifts in TG pigs, we measured body weight, detected serum indicators of lipid metabolism and glucose metabolism, and analyzed heart function in TG and WT pigs after 12 months of HFHSD intervention. Compared with those of WT pigs, the average body weight of TG pigs tended toward an increase, and the concentrations of high-density lipoprotein cholesterol (HDL-C) and insulin in the serum were significantly decreased. In addition, the serum glucose concentration appeared to be greater in TG samples (Figure 1A). However, we did not observe significant changes in cardiac enzymes in TG pigs (Table S1). Overall, compared with healthy controls, TG pigs exhibited disturbances in lipid metabolism and impaired insulin secretion after HFHSD induction, suggesting increased sensitivity to energy overload.

The M-mode echocardiography was performed to assess differences in the cardiac morphology and function of TG pigs. Although no differences were observed in the cardiac structure, TG pigs tended to have lower ejection fraction (%) (EF) compared with those from controls ($p = 0.055$) (Figure 1B, Table S2).

The pathological evaluation was performed on the left ventricle, interventricular septum and aortic vessel of TG and WT pigs. Hematoxylin and eosin (H&E) staining revealed that compared with those of WT group, the left ventricles of TG group manifested extensive edema, and some of the myofibers in the interventricular septum myocardium were ruptured (Figure 1C, top and middle panel). The aortic vessel wall displayed mild intimal edema and loss of arrangement of collagen fibers (Figure 1C, bottom). Furthermore, transmission electron microscopy revealed that compared with those in WT group, the integrity of mitochondria in TG group was impaired, as the inner membrane and cristae were damaged. Moreover, the linear mitochondrial registry was absent, and the mitochondria dissociated from the sarcomeres, thereby increasing the intracellular space. In addition, myofibrils were fragmented in TG samples (Figure 1D). Overall, cardiac injury caused by metabolic disorders is characterized by cardiomyocyte (CM) edema and mitochondrial damage, preceding the onset of overt cardiac dysfunction.

Cellular landscape of WT and TG pig hearts revealed by snRNA-seq

Next, to explore the cardiac cellular and transcriptional landscape in healthy and metabolic disorder conditions, left ventricular free walls (previous data have shown that metabolic abnormalities have a strong impact on left ventricular structure and function[14]) were collected from a WT pig and a TG pig and subjected to snRNA-seq analysis using 10× Genomics (Figure 2A). After strict quality control (QC), the final dataset consisted of 15,528 nuclei from WT sample and 13,217 nuclei from TG sample. WT sample had a median depth and median number of genes per cell of 29,426 reads and 2,033 genes, respectively, whereas the corresponding numbers for TG sample were 34,915 reads and 1,814 genes, respectively. We identified and visualized ten major cell types by canonical cell-specific marker genes,[4] including CMs, ECs, FBs, myeloid cells (MDs) (mainly MACs), T cells, pericytes (PCs), smooth muscle cells (SMCs), neuronal cells (NCs), erythroid cells (ERYs), and adipocytes (ADs) (Figures 2B, 2C, and S1A). Each population displayed distinct signature genes and consisted of cells from both WT and TG samples (Figure 2B, right, and Table S3). Consistent with humans, CMs, ECs, FBs, and MDs were the numerically dominant porcine cardiac cell types, accounting for 90% of the total number of cells in our data[4] (Figure 2D). The major cell types in pigs and humans exhibited highly conserved transcriptome signatures and shared common marker gene sets, according to a correlation analysis[15] (Figure 2E).

We observed changes in cardiac cell composition as a function of metabolic disorders. Although there were no differences in cell types between the two pigs, TG pig possessed fewer CMs and MDs, but more ECs (Figures 2D and S1B). Furthermore, the differentially expressed genes (DEGs) were screened based on the criteria of $p < 0.05$ and the fold change > 1.28 in each cell type between WT and TG samples (Figure 2F). Our data showed that except for ERYs, there are more than 1,000 DEGs in each cell type, suggesting the effect of metabolic disorders on gene expression in cardiac cell populations. (Figure 2F). We also generated bulk RNA sequencing (bulk RNA-seq) data for the same experimental group ($n = 3$ per group) to verify the representativeness of the snRNA-seq data. Spearman's correlation analysis revealed that the group DEGs of the major cell populations were significantly positively correlated with the bulk RNA-seq results ($p < 0.05$, fold change > 1.28) (Figure S1C, Table S3). As CMs, ECs, MDs, and FBs are the major cell types in the heart and there are many DEGs identified in these cells between the two samples, we next focused on the molecular signatures of these cardiac populations.

Metabolically active cardiomyocyte loss and dysfunction in TG pigs

CMs were identified by the general CM markers *ACTN2*, *RYR2*, and *FHL2*[4] (Figure 2C). To gain further insight into the function of each CM subtype, we classified CMs into five subsets (CM1–5) (Figure 3A, Table S4). Based on similarities in transcriptional patterns, we found that CM1, CM2, and CM4 share similar gene programs (Figure 3B). All three subtypes share many upregulated genes related to muscle development and muscle contraction, and display typical CM properties[16] (Figures 3C and 3E). Interestingly, the heterogeneous subset CM3 exhibited a highly energetic state with robust expression of mitochondrial genes (both nuclear-encoded and mitochondrial-encoded), and its Gene Ontology (GO) terms were enriched in oxidative phosphorylation and ATP synthesis. In addition, CM3 abundantly expressed genes encoding sarcomere protein, antioxidant heat shock protein and transcription factors (Figures 3D, 3E, and S2A), suggesting that this type of CM might be capable of performing a greater workload than others.

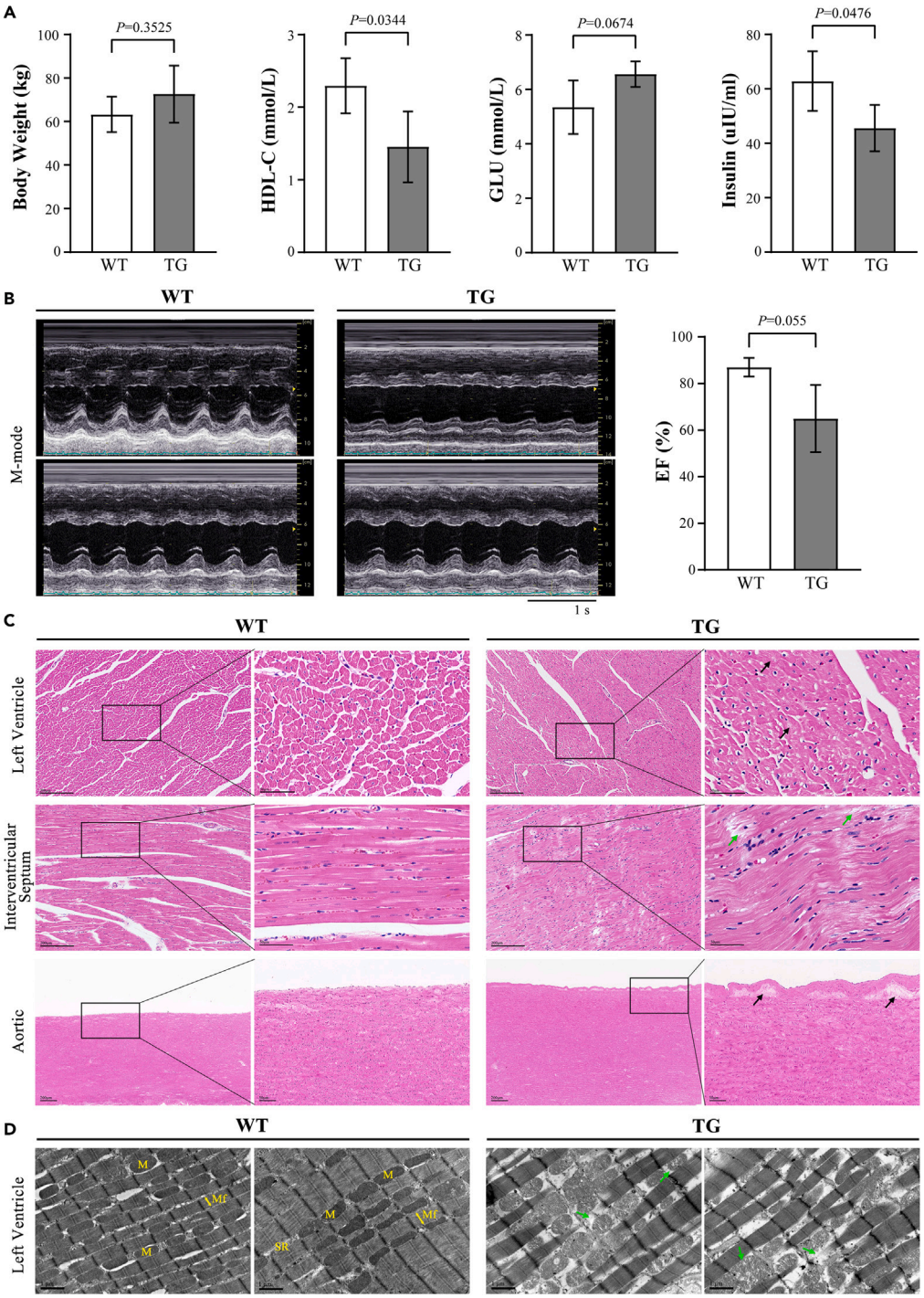

Figure 1. Clinical characteristics of TG pigs

(A) Average body weight and serum biochemical parameters. WT, wild-type group; TG, triple-transgenic group. HDL-C, high-density lipoprotein cholesterol; GLU, glucose.

(B) Representative images of echocardiography of left ventricle in WT and TG groups (left). Left ventricular ejection fraction (EF) of WT and TG groups (n = 3 per group) (right).

(C) Representative H&E staining images of left ventricle (top), interventricular septum (middle), and aortic vessel (bottom) of WT and TG pigs. The areas indicated by boxes are magnified on the right. Edema (black arrows) and myofiber rupture (green arrows) were indicated. Scale bars, 200 μm (left), 50 μm (right).

(D) Representative images of cardiac mitochondrial morphology obtained from electron microscope. Normal (yellow arrow) and damaged (green arrow) myocardial ultrastructure were indicated. M, mitochondria; Mf, myofibril; SR, sarcoplasmic reticulum. Scale bars, 1 μm.

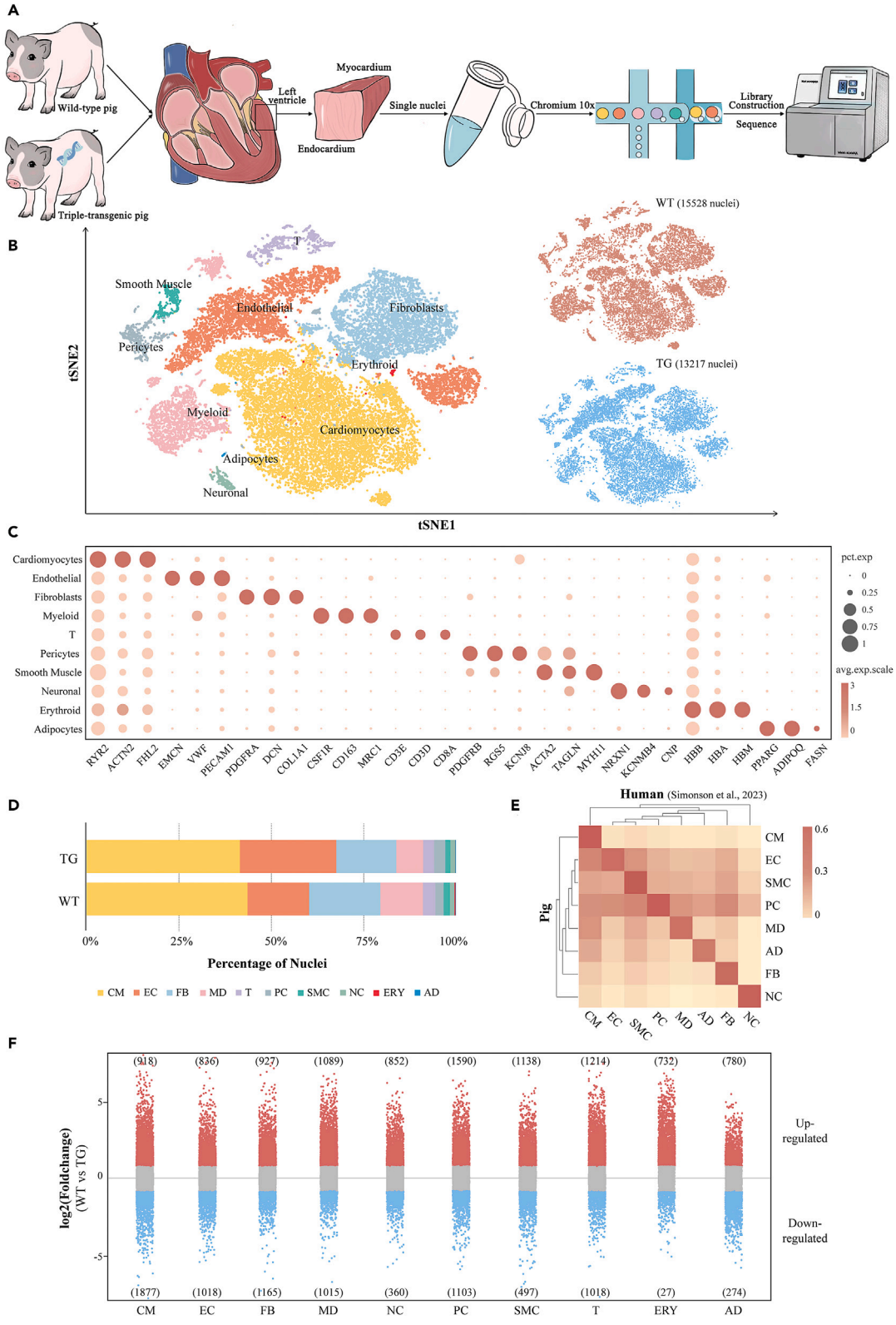
A
Wild-type pig
Triple-transgenic pig
Left ventricle
Myocardium
Endocardium
Single nuclei
Chromium 10x
Library Construction
Sequence
B
WT (15528 nuclei)
TG (13217 nuclei)
T
Smooth Muscle
Endothelial
Fibroblasts
Pericytes
Erythroid
Myeloid
Cardiomyocytes
Adipocytes
Neuronal
tSNE2
tSNE1
C
Cardiomyocytes
Endothelial
Fibroblasts
Myeloid
T
Pericytes
Smooth Muscle
Neuronal
Erythroid
Adipocytes
RYR2 ACTN2 PHL2 EMCN VWF PECAM1 PDGFRA DCN COL1A1 CSF1R CD163 MRC1 CD3E CD3D CD8A PDGFRB RGS5 KCNJ8 ACTA2 TAGLN MYH11 NRXN1 KCNMB4 CNP HBB HBA HBM PPARG ADIPOQ FASN
pct.exp
0
0.25
0.5
0.75
1
avg.exp.scale
3
1.5
0
D
TG
WT
0%
25%
50%
75%
100%
Percentage of Nuclei
CM EC FB MD T PC SMC NC ERY AD
E
Human (Simonson et al., 2023)
Pig
CM
EC
SMC
PC
MD
AD
FB
NC
0.6
0.3
0
F
log2(Foldchange) (WT vs TG)
5
0
-5
(918) (836) (927) (1089) (852) (1590) (1138) (1214) (732) (780)
(1877) (1018) (1165) (1015) (360) (1103) (497) (1018) (27) (274)
CM EC FB MD NC PC SMC T ERY AD
Up-regulated
Down-regulated

Figure 2. Cellular composition of WT and TG pig hearts

(A) Schematic of snRNA-seq experimental design and workflow. Transmural samples were obtained from left ventricle of wild-type (WT) and triple-transgenic (TG) pigs (n = 1 WT, n = 1 TG), single nuclei were processed using Chromium 10× 3′DEG chemistry.

(B) t-distributed stochastic neighbor embedding (t-SNE) clustering of 28,745 nuclei isolated from both WT and TG, split by cell type (left) or by source (right). Each dot represents a single cell.

(C) Known marker genes for each cell type. Dot color and size indicate the relative mean expression level and proportion of cells expressing the gene in each cell type, respectively.

(D) The proportion of cells within WT and TG hearts identified from nuclei. CM, (ventricular) cardiomyocytes; EC, endothelial cells; FB, fibroblasts; MD, myeloid cells; T, T cells; PC, pericytes; SMC, smooth muscle cells; NC, neuronal cells; ERY, erythroid cells; AD, adipocytes.

(E) Correlation matrix between pig and human cardiac cells. Normalized average UMI values for each cell type were used in the calculation of correlation coefficient values.

(F) Dot plots showing the number of up- and downregulated genes in TG cardiac cells relative to WT group ($p < 0.05$, fold change > 1.28).

To characterize CMs under metabolic disorder conditions, we examined the global transcriptional changes in CMs between TG and WT groups. We observed that a large number of structural genes (such as *ACTC1*, *TNNT2*, *MYL3*, and *MYBPC3*) were significantly downregulated in TG sample (Figure S2B). Pathways involved in muscle contraction, fatty acid metabolism, and oxidative phosphorylation were downregulated in TG group (Figure S2C), consistent with the observed decrease in cardiac function. This result was also further confirmed by bulk RNA-seq (Figure S2D). We further analyzed the proportional changes in each CM subtype between the two groups and found that the cellular abundance of CM3 was markedly decreased in TG (Figure 3F, Table S4). Thus, we selected TPT1 as the specific marker for CM3 (due to the wide expression of mitochondrial genes in various cell types) and colocalized it with TNNT2 (a general CM marker) to validate the reduction of CM3 in TG sample (Figures 3G and S2E). More importantly, the expression of CM3 signature genes (sarcomere generation genes and mitochondrion-related genes) was significantly reduced in TG pig, and numerous metabolism-related genes (mainly glycolysis and TCA cycle-related genes) were also markedly downregulated in TG sample (Figure 3H, Table S4). Furthermore, pathway enrichment analysis of DEGs in CM3 (comparing WT to TG) revealed a significant downregulation of oxidative phosphorylation, metabolism and cardiac muscle contraction processes in TG sample compared with WT (Figure 3I). Together, these findings highlight the presence of multiple CM subtypes, and metabolically active CMs were strongly influenced in metabolic disorders.

Activation of proinflammatory endothelial cells with leukocyte recruitment potential in TG pigs

Seven EC subsets were identified in our data, characterized by high expression of pan-EC markers (*VWF*, *PECAM1*, and *EMCN*)[4] (Figures 4A and 2C, and Table S5), most of which were blood vascular ECs (BECs) (accounting for 74.4% of all ECs) and a small portion of lymphatic ECs (Table S5). We further assigned endothelial subtype classifications for all BECs. Capillary-EC co-expressed the capillary markers *CA4* and *RGCC*[17] and lipid metabolism-related genes (*CD36*, *FABP4*, and *FABP5*),[18] implying potential lipid regulatory properties (Figures 4B and S3A). Arterial-EC was enriched for mature arterial markers *GJA5* and *SEMA3G*[17] (Figures 4B and S3A). Angiogenic-EC highly expressed the developmental angiogenesis regulator *HEY1*,[19] and its biological function was mainly involved in angiogenesis (Figures 4B, 4C, and S3A). We observed two distinct proinflammatory-EC subsets that specifically expressed genes related to immune regulation, including *ACKR1*, *PLVAP*, and *CCL14*,[10] and their GO terms were enriched in leukocyte migration and antigen presentation processes (Figures 4B, 4C, and S3A). Compared with proinflammatory-EC1, proinflammatory-EC2 has a specific expression on *EPHB1* and *CA8*, indicating its potential ability to regulate EC migration[20,21] (Figures 4B, 4C, and S3A). Contractile-EC abundantly expressed sarcomere protein genes, while lymphatic-EC specifically expressed the lymphatic markers *LYVE1*, *MMRN1*, and *RELN*[17] (Figure 4B).

We observed globally upregulated expression of stress-response genes (such as *ANKRD1* and *TXNIP*) and interferon-stimulated genes (*ISG15*, *IFI6*, and *IFI44*) in all BEC subsets of TG group,[22,23] and this phenomenon was supported by bulk RNA-seq (3 WT hearts and 3 TG hearts) (Figure 4D). Genes encoding heat shock proteins (*HSPB6*, *HSPB7*, and *CRYAB*) and fatty acid binding proteins (*FABP3*, *FABP4*, and *FABP5*), which were reported to be positively correlated with cardiovascular events,[24,25] were also significantly upregulated in TG, compared with WT (Figure S3B).

As reported in previous studies, ACKR1$^+$ ECs predominantly mediate inflammatory responses via leukocyte infiltration.[26,27] To test whether proinflammatory ECs (which specifically express *ACKR1*) are altered in metabolic disorders, the DEGs between the two groups were screened (Table S5). Our data revealed that both proinflammatory EC subsets exhibit an activation phenotype,[28] with proinflammatory-EC2 having the most robust activation profile (Figure S3C). In addition to the globally upregulated DEGs of all BECs, the expression of adhesion molecules, proinflammatory cytokines and inflammation-related transcription factors (including *VCAM1*, *ICAM1*, *CXCL10*, *TGFB1*, *CEBPB*, and *CEBPD*) was markedly increased in proinflammatory-EC2 from TG sample (Figure 4E, Table S5). We further confirmed VCAM1 expression in proinflammatory ECs in the TG heart by immunofluorescence staining (Figure 4F). GO analysis revealed that the regulation of leukocyte activation and adhesion by proinflammatory-EC2 in TG sample was markedly greater than that in WT (Figure 4E). Kyoto Encyclopedia of Genes and Genomes (KEGG) pathway analysis revealed the upregulation of multiple pathways associated with EC dysfunction in TG sample (such as the TGF-beta signaling pathway, AGE-RAGE signaling pathway, and fluid shear stress and atherosclerosis process)[29] (Figure S3D). Overall, these results suggest that the activation of ECs might be associated with metabolic disease-induced myocardial injury.

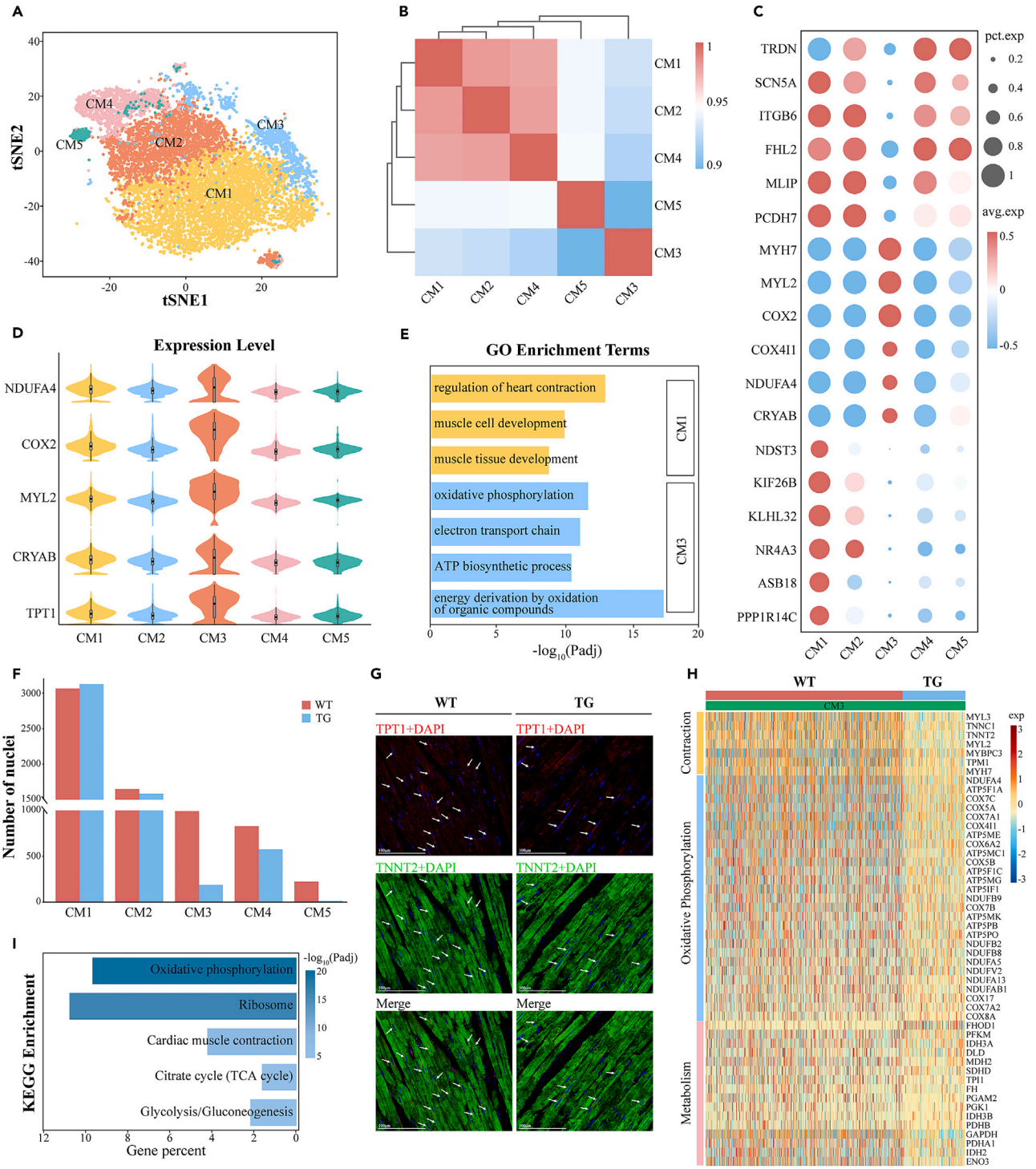

Figure 3. Cardiomyocyte subpopulations and their alterations in TG pigs

(A) t-SNE projection of five cardiomyocyte (CM) subpopulations.

(B) Heatmap showing correlation of five CM subpopulations by Spearman correlation analysis.

(C) Dot plot representing the signature gene expression in each CM subpopulation. Dot color and size indicate the relative mean expression level and proportion of cells expressing the gene in each subpopulation, respectively.

(D) Violin plots showing the expression of top distinct genes of CM3 subpopulation.

(E) Selected top GO enrichment terms for subcluster-specific genes of CM subpopulations.

Figure 3. *Continued*

(F) The number of CMs of each CM subpopulation in WT and TG samples.

(G) Co-staining of CM general marker TNNT2 and CM3 special marker TPT1 in left ventricular sections of WT sample, the white arrows indicate co-localized CMs (CM3). Scale bars, 100 μm.

(H) Heatmap showing the top differentially expressed genes (DEGs) in CM3 subpopulations comparing WT to TG.

(I) Significant downregulated KEGG pathways of CM3 subpopulation in TG group.

Reduction in the number of reparative LYVE1$^+$ tissue-resident cardiac macrophages in TG pigs

Analysis revealed the presence of eight MD populations in our data (Figures S4A and S4B). These MD populations were composed of large numbers of MACs (72.3%), including LYVE1$^+$ MAC1, MHC-II^{hi} MAC2, MAC3, and MAC4, and smaller numbers of monocytes (MOs), dendritic cells (DCs), and mast cells (Figure S4C, Table S6). MACs are heterogeneous cell populations, and separate subpopulations of MAC with distinct gene expression profiles, phenotypes, and functions exist in mice and humans.[30] Thus, we further focused on characterizing the four subtypes of MACs (Figure 5A). LYVE1$^+$ MAC1 was the most transcriptionally unique MAC subcluster expressing reparative RCM marker genes such as *LYVE1*, *FOLR2*, *MRC1*, and *VSIG4*.[31] MHC-II^{hi} MAC2 highly expressed genes involved in immune response activation and antigen presentation (the major histocompatibility complex class II encoding genes and *CX3CR1*) (Figure 5B). There are also two small subsets MAC3 and MAC4. MAC3 highly expressed a variety of cell surface receptors and genes related to the extracellular matrix (ECM), and MAC4 had a relatively higher expression of genes related to myocardial tissue growth and muscle contraction (Figure 5B).

We further examined the differences in enriched pathways between LYVE1$^+$ MAC1 and MHC-II^{hi} MAC2. The enriched pathways of LYVE1$^+$ MAC1 were related to homeostatic and regenerative functions. Tissue repair genes, such as *IGF1*, *MEF2A*, and platelet-derived growth factor family, were highly expressed in this subpopulation, and the DEGs were enriched in endocytosis, intracellular signal transduction, blood vessel development, and muscle cell proliferation processes. Compared with LYVE1$^+$ MAC1, MHC-II^{hi} MAC2 had more active immune-related pathways, including leukocyte activation, antigen presentation and interferon-γ response (Figures 5C and S4D).

We observed that in TG group, the major MAC subsets retained their characteristic gene expression and core transcriptional programs, and no additional MAC subclusters developed (Figures 5D and S4E). Importantly, the impact of metabolic disorders on MACs was manifested by a significant reduction in the abundance of reparative LYVE1$^+$ MAC1 (Figure 5E), and immunofluorescence staining further confirmed the depletion of LYVE1$^+$ MACs in TG hearts (Figure 5F). Furthermore, metabolic disorders induce small-scale transcriptional changes. Compared with those of WT, the upregulated genes in the LYVE1$^+$ MAC1 of TG sample were mapped to pathways involved in leukocyte migration and the response to lipopolysaccharide, and the MHC-II^{hi} MAC2 subset in TG sample was more enriched in pathways related to interferon-gamma and the Toll-like receptor signaling pathway. Additionally, the increased response to chemical stimuli was shared across subsets in TG (Figure 5G).

Increased fibroblast plasticity in TG pigs

Our data revealed that FBs robustly expressed general FB markers, such as *DCN*, *GSN*, and *PDGFRA*[4] (Figure 2C). We investigated the cellular composition of FBs, as FBs are the major contributors to cardiac fibrosis.[32] FBs can be further divided into six subtypes (FB1–6) (Figure 6A, Table S7). The FB1 and FB2 subsets comprised the majority of FBs, displaying a canonical expression program of FB, with high expression of genes encoding members of the ATP-binding cassette transporters superfamily (*ABCA6* and *ABCA8*) and non-collagenous constituent of ECM (Figures 6B and 6C). GO analysis revealed that the biological functions of FB1 and FB2 were related to cell migration and anatomical structure morphogenesis (Figure 6D). Several minor FB subpopulations had different characteristics. FB3 subset has higher expression of cytokine receptors and was enriched in enzyme-linked receptor protein signaling pathway. FB5 subset exhibited pro-fibrogenic signatures with specific expression of activated FBs markers (*POSTN*, *LTBP4*, *LUM*, *MGP*, and *THBS4*), and had maximal ECM synthesis properties (*COL1A1*, *COL1A2*, and *COL3A1*). By contrast, FB4 subset had lower expression of ECM-related genes, but it specifically expressed vascular endothelial growth factors and receptors such as *FLT1*, *EGFL7*, and *EPAS1*, and was enriched in blood vessel development process (Figure 6C and 6D).

All FB subtypes, including disease-associated FB5, were present in both WT and TG hearts (Figure 6E). To explore the diversity of cellular differentiation states in disease, we utilized single-cell lineage inference using cell expression similarity and entropy (SLICE)[33] and partition-based graph abstraction (PAGA)[34] to perform single-cell entropy calculations and pseudotime analysis on all FBs from WT and TG samples. Entropy is inversely proportional to the cell differentiation state, that is, high-entropy cells have more diverse expression patterns.[33,35] Compared with that in WT, the cellular differentiation state of FB1 in TG sample was lower (high entropy and low pseudotime values), indicating substantial plasticity of this population (Figure 6F). However, we did not observe an activation signature of cardiac fibrosis or increased cellular abundance in the FBs of TG sample.

Reduction in trophic intercellular interactions between noncardiomyocytes and cardiomyocytes in TG pigs

There is extensive intercellular communication in the normal heart, as previously reported.[36] To determine the regulatory relationship between cardiac cells in pigs and further reveal the changes in intercellular signaling in metabolic disorders, we mapped ligands and cognate receptors to subpopulations of major cardiac cell types, and constructed a cell interaction network via CellPhoneDB. ECs, FBs, and MACs were important populations that formed the potential signaling network within different cell types (Figure 7A). Widespread trophic intercellular interactions between cardiac cells have been reported;[5] therefore, we examined the expression of factors essential for supporting

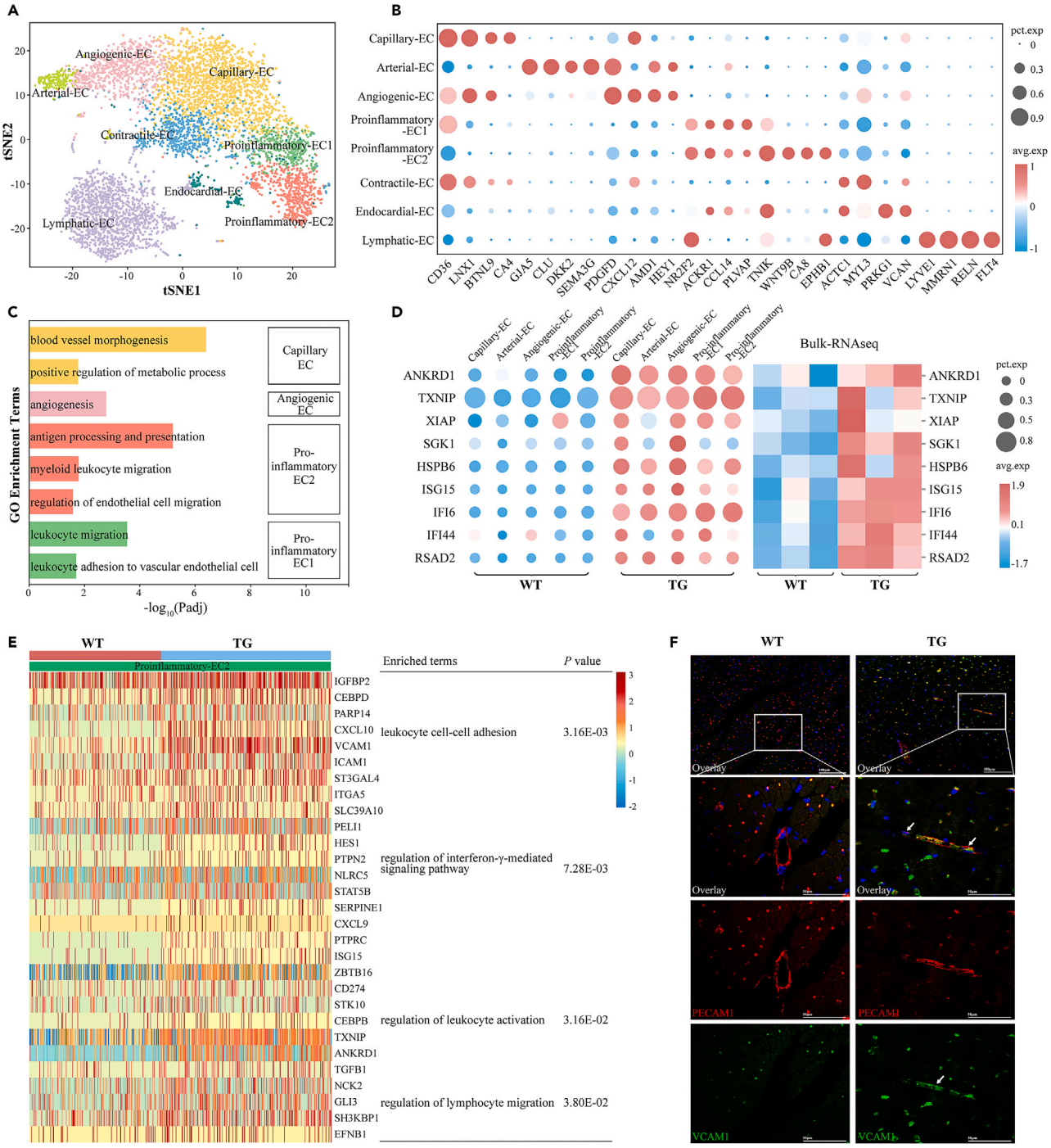

Figure 4. Endothelial cell subpopulations and their alterations in TG pigs

(A) t-SNE projection of seven endothelial cell (EC) subpopulations.

(B) Dot plot representing the signature gene expression in each EC subpopulation. Dot color and size indicate the relative mean expression level and proportion of cells expressing the gene in each subpopulation, respectively.

(C) Selected top GO enrichment terms for subcluster-specific genes of BEC subpopulations.

(D) Expression of key differentially expressed genes (DEGs) in all BECs subpopulations and bulk RNA-seq data.

(E) Heatmap showing the top DEGs (left) and their enriched GO terms (right) in proinflammatory-EC2 subpopulations comparing WT to TG.

(F) Co-staining of VCAM1 and general EC marker PECAM1 in WT versus TG sections. Scale bar, 100 μm (top), 50 μm (bottom).

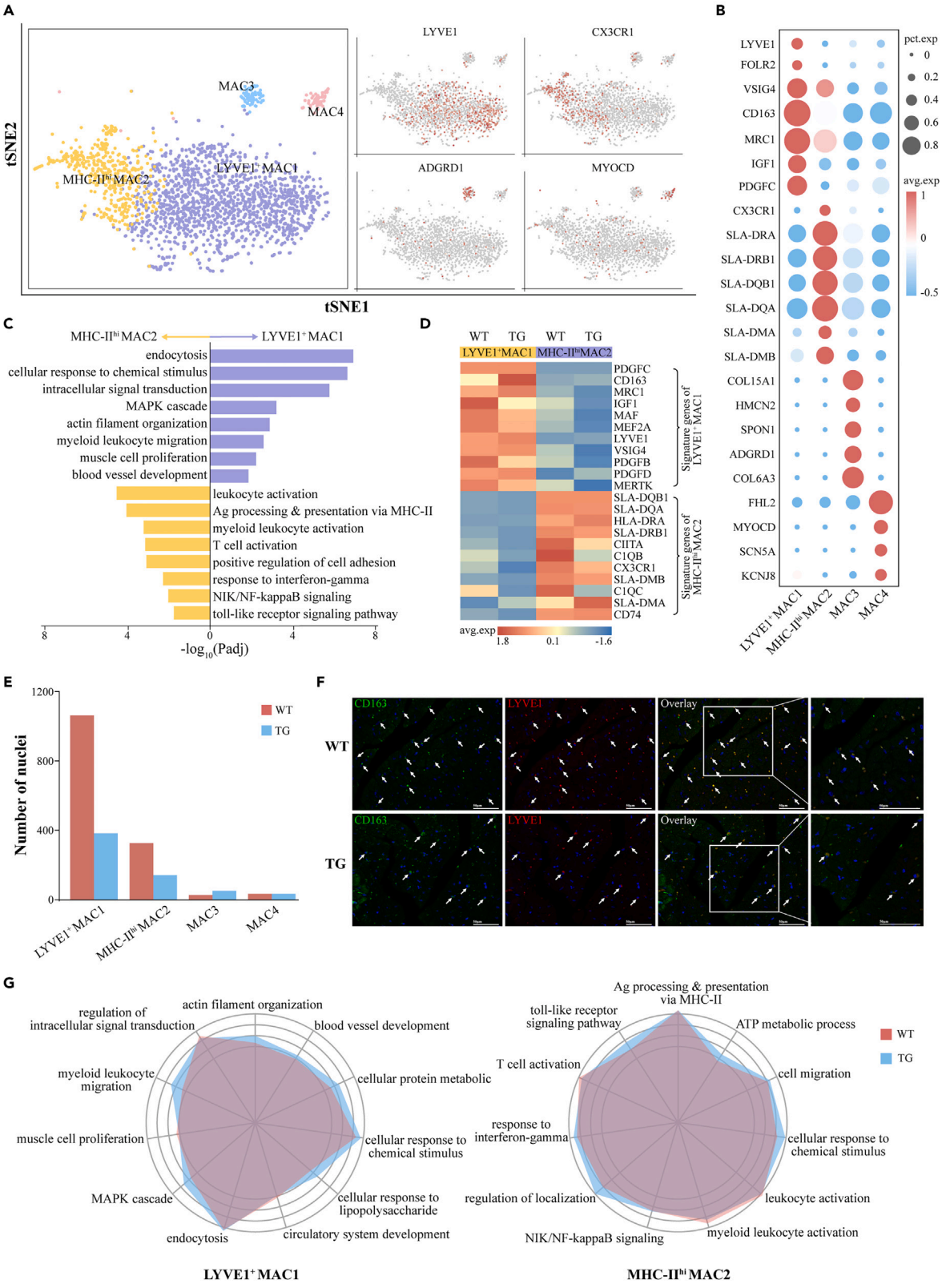
A
tSNE2
tSNE1
MAC3
MAC4
MHC-II^hi MAC2
LYVE1+ MAC1
LYVE1
CX3CR1
ADGRD1
MYOCD
B
LYVE1
FOLR2
VSIG4
CD163
MRC1
IGF1
PDGFC
CX3CR1
SLA-DRA
SLA-DRB1
SLA-DQB1
SLA-DQA
SLA-DMA
SLA-DMB
COL15A1
HMCN2
SPON1
ADGRD1
COL6A3
FHL2
MYOCD
SCN5A
KCNJ8
pct.exp
0
0.2
0.4
0.6
0.8
avg.exp
1
0
-0.5
LYVE1+MAC1
MHC-II^hi MAC2
MAC3
MAC4
C
MHC-II^hi MAC2
LYVE1+ MAC1
endocytosis
cellular response to chemical stimulus
intracellular signal transduction
MAPK cascade
actin filament organization
myeloid leukocyte migration
muscle cell proliferation
blood vessel development
leukocyte activation
Ag processing & presentation via MHC-II
myeloid leukocyte activation
T cell activation
positive regulation of cell adhesion
response to interferon-gamma
NIK/NF-kappaB signaling
toll-like receptor signaling pathway
8
4
0
4
8
-log10(Padj)
D
WT
TG
WT
TG
LYVE1+MAC1
MHC-II^hi MAC2
PDGFC
CD163
MRC1
IGF1
MAF
MEF2A
LYVE1
VSIG4
PDGFB
PDGFD
MERTK
SLA-DQB1
SLA-DQA
HLA-DRA
SLA-DRB1
CIITA
C1QB
CX3CR1
SLA-DMB
C1QC
SLA-DMA
CD74
Signature genes of LYVE1+ MAC1
Signature genes of MHC-II^hi MAC2
avg.exp
1.8
0.1
-1.6
E
Number of nuclei
1200
800
400
0
WT
TG
LYVE1+MAC1
MHC-II^hi MAC2
MAC3
MAC4
F
WT
TG
CD163
LYVE1
Overlay
G
actin filament organization
blood vessel development
cellular protein metabolic
cellular response to chemical stimulus
cellular response to lipopolysaccharide
circulatory system development
endocytosis
MAPK cascade
muscle cell proliferation
myeloid leukocyte migration
regulation of intracellular signal transduction
LYVE1+ MAC1
Ag processing & presentation via MHC-II
ATP metabolic process
cell migration
cellular response to chemical stimulus
leukocyte activation
myeloid leukocyte activation
NIK/NF-kappaB signaling
regulation of localization
response to interferon-gamma
T cell activation
toll-like receptor signaling pathway
MHC-II^hi MAC2
WT
TG

Figure 5. Macrophage subpopulations and their alterations in TG pigs

(A) t-SNE projection of four macrophage (MAC) subpopulations (left) and their selected signature genes (right).

(B) Dot plot representing the selected marker gene expression in each MAC subpopulation. Dot color and size indicate the relative mean expression level and proportion of cells expressing the gene in each subpopulation.

(C) Selected top GO enrichment terms for subcluster-specific genes of major MAC subpopulations.

(D) Heatmap showing the average expression of marker genes of LYVE1^{+} MAC1 and MHC-II^{hi} MAC2 obtained from WT or TG samples, respectively.

(E) The number of macrophages of each MAC subpopulation in WT and TG samples.

(F) Co-staining of MAC1-specific marker LYVE1 and MAC pan-marker CD163, the white arrows indicate co-localized MACs. Scale bar, 50 μm.

(G) Radar plot showing GO enrichment terms of highly expressed genes of major MAC subpopulations in WT and TG groups. Left, LYVE1^{+} MAC1, right, MHC-II^{hi} MAC2.

specific cell types in different cardiac cell populations (Figure 7B). In addition to the previously reported trophic effects of FBs on multiple cardiac cell types, the LVYE1^{+} MAC1 subpopulation was identified as the most highly enriched for *IGF1* transcripts, required to maintain CM adaptive growth[36,37] (Figure 7B). An examination of ligands released by significantly altered cell subpopulations (metabolically active CM3, LVYE1^{+} MAC1, and proinflammation-EC2) revealed important intercellular interactions among them (Figure 7C, Table S8). Besides the trophic effect (such as IGF1-IGF1R), through GAS6/MERTK, LVYE1^{+} MACs may recognize apoptotic CMs and efferocytosis to resolve inflammation.[38] Proinflammatory-ECs secrete a variety of inflammatory mediators such as *LGALS9* and *MIF*, which play an important role in the pathogenesis of inflammation in CVDs[39,40] (Figure 7C).

Metabolic abnormalities potentially influence cardiac intercellular signaling. Thus, we examined the expression of ligands and their corresponding receptors released by these altered cell subtypes and compared the differences between WT and TG samples. We found that a multitude of trophic ligands including *IGF1*, *IGF2*, and *NRG4* secreted from proinflammatory-EC2 and LYVE1^{+} MAC1 were significantly reduced in TG pig, which may affect the abundance and morphological maintenance of CMs[37,41] (Figure 7D). Moreover, *WNT2* transcripts was significantly upregulated in the proinflammatory-EC2 of TG sample, possibly regulating LYVE1^{+} MAC1 polarization through WNT2/FZD3[42] (Figure 7D).

DISCUSSION

Accumulating studies have revealed the complex composition of cardiac cells in healthy adult human hearts and further investigated the dynamic changes in cardiac cells under limited cardiac function conditions. However, due to the limited access to human heart samples, studies on cardiac injury caused by metabolic diseases at single-cell resolution are lacking. The widespread use of pigs in translational cardiovascular research inspired us to use a recently characterized transgenic minipig model of metabolic disease as material to explore how metabolic diseases affect cardiac cell composition and cell type-specific transcriptional programs. After 12 months of HFHSD intervention, the transgenic pigs had reduced HDL-C levels and exhibited a tendency toward increases in body weight and serum glucose levels, consistent with human MetS.[43] Cardiac function was not significantly altered in TG pigs, possibly due to the limited impact of early metabolic disease on cardiac function, which was also observed in obese adolescent patients and early-MetS pig models.[44,45] However, impaired mitochondrial distribution and morphology could already be observed in TG myocardial samples, consistent with studies of early-stage MetS.[44] These impairments in the early stage may later initiate and further promote cardiac dysfunction.

Using snRNA-seq, we obtained insight into the cell composition of healthy and metabolic disorder porcine cardiac tissue samples and identified ten major cell types, covering most of the cell types previously reported in human and mouse studies.[4,46] Furthermore, we uncovered the compositional shifts in CMs and MACs, and transcriptional alterations in CMs and ECs in TG pig heart.

Previous scRNA-seq studies of mammalian hearts have excluded CMs because energy-sensitive CMs die rapidly after isolation, and the huge size of CMs are unsuitable for conventional single-cell platforms.[9] Therefore, we applied snRNA-seq technology to avoid the problems of cell isolation and cell size differences. Consistent with findings from recent single-cell analyses in developing and adult mammalian hearts, we found that ventricular CMs also contained heterogeneous cell subpopulations.[4,9,16] In addition to canonical ventricular CMs, there was a metabolically active CM subpopulation with high expression of genes related to energy metabolism, sarcomere proteins and heat shock proteins. Previous single-cell studies have demonstrated a similar subpopulation in normal adult hearts, possibly suggesting that the diversity of ventricular CMs is conserved across species.[4]

We further found that the metabolic state strongly influenced the composition and gene expression of CMs. Collectively, CMs in cardiac injury induced by metabolic disorders converge toward a common disease-associated state. Compared with those in WT, CMs in TG group exhibited a global decrease in the expression of structural genes associated with cardiac function (such as *MYL2*, *MYL3*, *MYBPC3*, *TNNT2*, and *ACTN2*), consistent with the findings in DCM patients.[7] We observed considerable variation in the responses of different CM subpopulations to metabolic disorders. In addition to the downregulation of structural genes in metabolically active CM3 subset, the expression of mitochondrial-related genes was also significantly decreased, concordant with our previous observation of mitochondrial damage in TG hearts. Moreover, relative to that of WT sample, the CM abundance of TG was generally reduced, especially the selective loss of metabolically active CM3. Recent research on myocardial infarction (MI) patients has indicated that the loss and/or dysfunction of CMs impairs heart contraction.[47] Therefore, metabolic abnormalities lead to myocardial injury, especially dysfunction or depletion of metabolically active CMs, which may further contribute to cardiac functional decline. Further clarification of the initiating mechanisms of these alterations will provide opportunities to intervene in metabolic disease-related cardiovascular events.

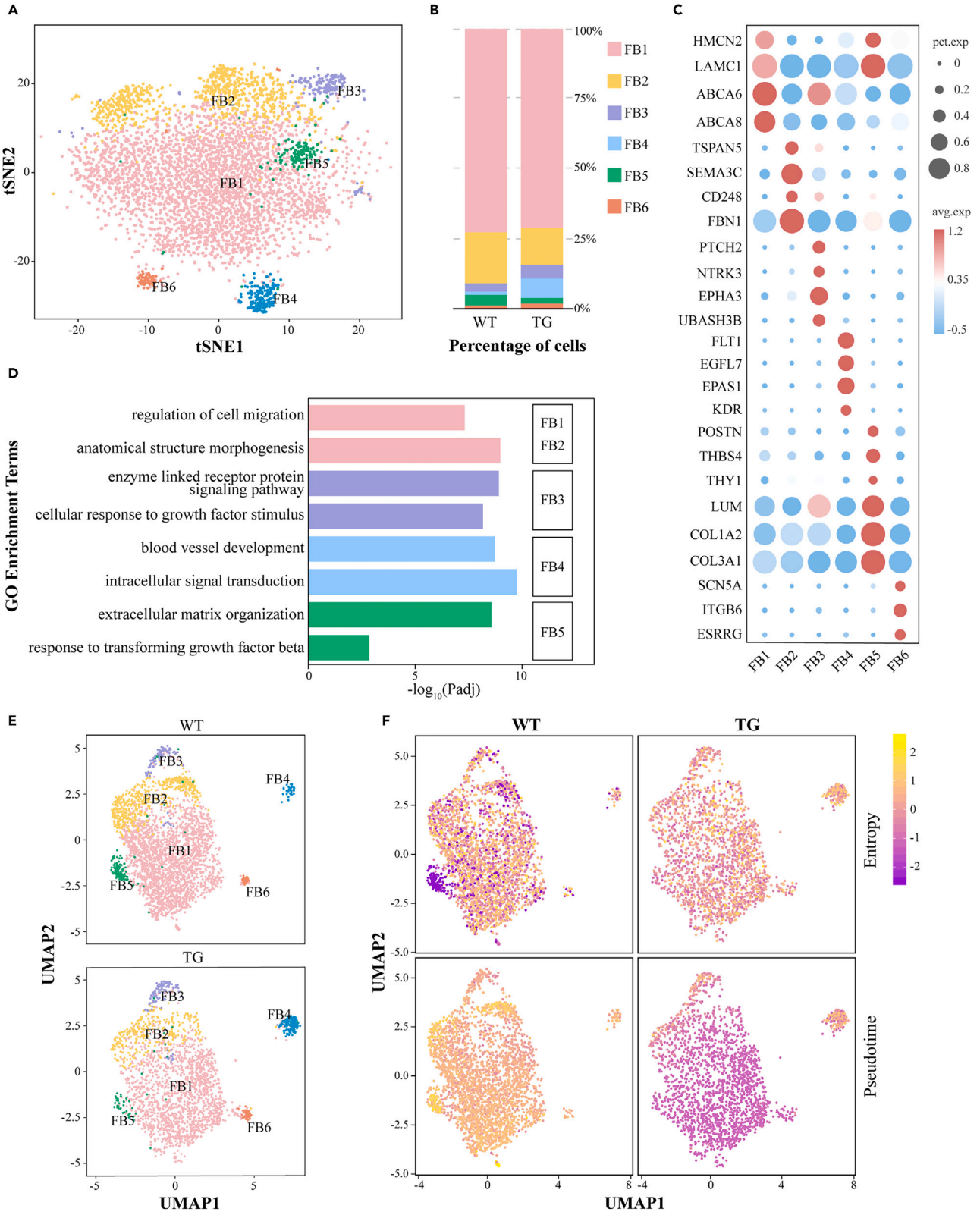
A
tSNE2
tSNE1
FB1
FB2
FB3
FB4
FB5
FB6
B
100%
75%
50%
25%
0%
WT
TG
Percentage of cells
C
HMCN2
LAMC1
ABCA6
ABCA8
TSPAN5
SEMA3C
CD248
FBN1
PTCH2
NTRK3
EPHA3
UBASH3B
FLT1
EGFL7
EPAS1
KDR
POSTN
THBS4
THY1
LUM
COL1A2
COL3A1
SCN5A
ITGB6
ESRRG
pct.exp
avg.exp
D
GO Enrichment Terms
regulation of cell migration
anatomical structure morphogenesis
enzyme linked receptor protein signaling pathway
cellular response to growth factor stimulus
blood vessel development
intracellular signal transduction
extracellular matrix organization
response to transforming growth factor beta
-log10(Padj)
E
WT
TG
UMAP2
UMAP1
F
WT
TG
Entropy
Pseudotime
UMAP2
UMAP1

Figure 6. Fibroblast subpopulations and their alterations between WT and TG pigs

(A) t-SNE projection of six fibroblast (FB) subpopulations.

(B) The proportion of FB subpopulations in WT and TG pigs identified from nuclei.

(C) Dot plot representing the signature gene expression in each FB subpopulation.

(D) Selected top GO enrichment terms for subcluster-specific genes of FB subpopulations.

(E) UMAP (Uniform Manifold Approximation and Projection) projection of FB populations split by source.

(F) Entropy and pseudotime overlayed on UMAP projection split by source.

We observed compositional and transcriptional changes in NCM populations (MACs and ECs) between healthy controls and metabolic disorder model pigs. As a central cellular component of the human myocardium, ECs regulate inflammatory responses by modulating leukocyte infiltration in diseased hearts.[48] Activated ECs, known to have leukocyte-recruiting potential, are abundant in HF patients and are characterized by the notable expression of *ACKR1* and cell adhesion molecules.[28,49] We detected similar activation signature that included *VCAM1*, *ICAM1* (mediating leukocyte-endothelial cell adhesion), *CXCL10* (regulating leukocyte recruitment), and *CEBPD* (involved in activating the transcription of multiple inflammatory genes),[50] which were selectively expressed in ACKR1$^+$ proinflammatory ECs in TG group. Furthermore, the ability of proinflammatory EC2 to mediate leukocyte adhesion was markedly enhanced in TG sample. Analysis of the DEGs indicated that *TXNIP*, *ANKRD1*, and *FABP4* were significantly upregulated in TG group. Overexpression of *TXNIP* leads to increased secretion of *VCAM1* and *ICAM1* through the *TXNIP/TRX/ASK1* pathway, simultaneously inhibiting *KLF2* expression and thus promoting EC inflammation.[51,52] *FABP4* activates the adhesion of ECs to monocytes to increase the risk of atherosclerosis, and blocking *FABP4* attenuates the expression of *ICAM1*, *VCAM1*, and *SELP*.[25] Increased *ANKRD1* expression was found in cardiac hypertrophy and DCM patients.[7,53] These observations suggest that EC phenotypic transformation in diseased hearts may be triggered by the overexpression of *TXNIP* and *FABP4*.

MACs are the most abundant immune cells in the heart and can be briefly divided into embryonic-derived and monocyte-derived sources. Embryonic-derived RCMs account for approximately 70% of the total MACs within the normal human heart, and are responsible for maintaining cardiac environmental homeostasis.[31,37] Recent single-cell analyses of human and mouse heart have suggested that RCMs can be categorized into at least three subsets according to the core gene program and life cycle: the TLF$^+$ cluster (*TIMD4*$^+$ *LYVE1*$^+$ *MHC-II*^{lo} *CCR2*$^-$), the MHC-II^{hi} cluster (*TIMD4*$^-$ *LYVE1*$^-$ *MHC-II*^{hi} *CCR2*$^-$) and the CCR2$^+$ cluster (*CCR2*$^+$*MHC-II*^{hi}). The TLF$^+$ cluster was prominent in homeostatic and regenerative functions, whereas the MHC-II^{hi} cluster was prominent in immune regulation.[30,54] Our data identified multiple heterogeneous MAC subsets, consisting of four cellular populations marked by *LYVE1*, *MHC-II*, *ADGRD1*, and *MYOCD* expression. Notably, the LYVE1$^+$ subset has a transcriptional signature similar to that of the human TLF$^+$ subpopulation, which characteristically expresses TLF$^+$ markers such as *LYVE1*, *FOLR2*, *VSIG4*, *MRC1*, and *IGF1*, and its biological functions are also related to vascular and muscle development.[37,55] However, the LVYE1$^+$ subpopulation in our study was negative for *TIDM4*. This is possibly because *TIDM4* expression was mainly restricted to the fetal heart and was significantly decreased in adulthood.[56] In addition, the MHC-II^{hi} subset in our study had relatively high expression levels of antigen-presenting genes (such as *SLA-DQA* and *SLA-DQB1*), consistent with MHC-II^{hi} clusters in humans and mice.[57] Overall, we found RCM subpopulations in the pig hearts that were similar to those previously demonstrated in humans and mice, suggesting the existence of a generalized framework across species to define the identity of MACs.

It is well known that RCMs greatly contribute to organ development,[58] CM energetics,[59] and compensatory remodeling in disease.[60] We found that the abundance of LYVE1$^+$ RCMs, which are characteristic of tissue repair, was markedly lower in TG sample than in WT, despite the lack of alterations in the core transcriptional pattern. This finding was also evident in mouse models of cardiac injury,[61,62] as well as in patients with HF or MI.[7,30] Recent studies on RCM functions have demonstrated that RCMs participate in cardiac regeneration and adaptive remodeling through the secretion of factors that act on CMs. RCM-derived CCL24 induced neonatal CM proliferation in MI.[62,63] During hypertension, RCMs promoted the adaptive growth of adult CMs via IGF-1 secretion, and the inducible ablation of RCMs with the Cx3cr1^{creERT2}-depletion system resulted in contractile dysfunction and myocardial fibrosis.[37] We speculate that the depletion of reparative RCM may contribute to the loss of CMs in metabolically disordered hearts.

In conclusion, we characterized the histopathological features of metabolic disease-induced cardiac injury and comprehensively analyzed the cellular transcriptomic landscape in healthy and metabolically impaired porcine cardiac tissue at the single-cell level. Our findings can be summarized into three points. (1) The early stages of metabolic disease-induced cardiac injury are characterized by tissue edema and mitochondrial damage, despite preserved cardiac function. (2) Pigs share a cardiac cell atlas similar to that of humans at the single-cell level. (3) Metabolically active CM dysfunction with abundance reduction, reparative MAC (or RCM) depletion, and proinflammation-EC phenotypic remodeling are closely associated with cardiac damage induced by metabolic diseases. Collectively, our findings extend the understanding of the impact of metabolic diseases on the heart and provide a reference for early disease intervention.

Limitations of the study

We recognize that this study still has several limitations. Although we have characterized the cellular landscape of healthy and metabolically disordered porcine hearts at the single-cell level, the complete diversity contained within the heart may not be fully reflected due to limitations in sample size and sample collection location. If individual- and location-based transcriptional differences exist, it may introduce unintended bias into this study. Furthermore, the transgenic models we used in this study were at early-stage of disease, and our comparison of molecular pathological changes in certain cell types may be limited. Future research will expand the number of normal and diseased tissue comparisons and will focus on exploring the delicate triggers of EC activation and initiating factors of reparative MACs depletion.

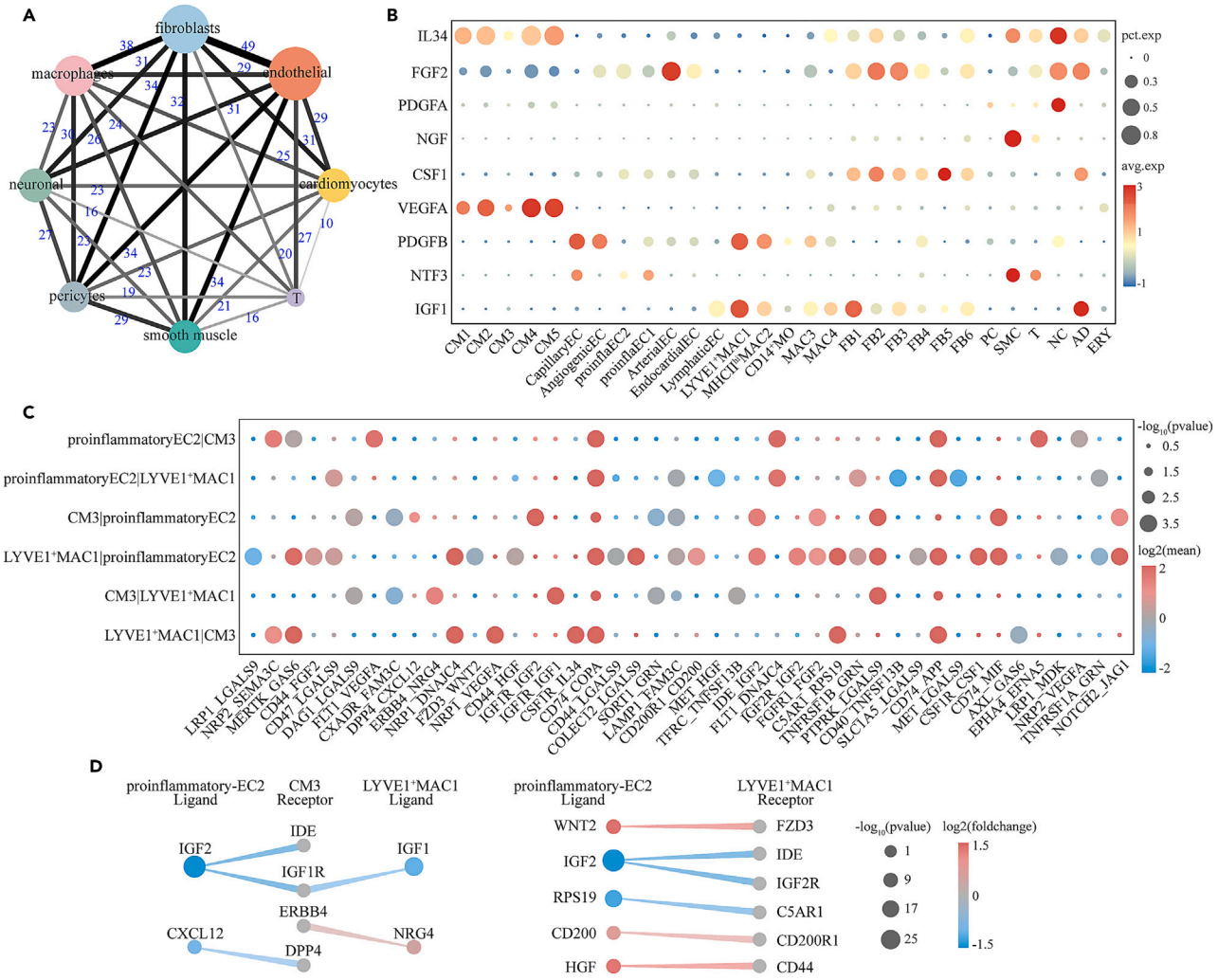

Figure 7. Intercellular connection network of cardiac cells

(A) Network of cell-cell interactions in cardiac cells, dot color indicates the cell type, dot size indicates the total number of significant ligand-receptor pairs of each cell type, line thickness indicates the number of significant interactions between two cell types.

(B) Dot plot representing the selected essential growth factors expression in major cardiac cell (sub)types.

(C) Dot plot shows significant ligand-receptor pairs between changed cardiac cell subtypes.

(D) Line plot showing ligands secreted by changed noncardiomyocyte subsets and their matching receptors. Dot color and size indicate the fold change and *p* value of the ligand in the subpopulation of TG group, respectively.

STAR★METHODS

Detailed methods are provided in the online version of this paper and include the following:

- KEY RESOURCES TABLE
- RESOURCE AVAILABILITY
  - Lead contact
  - Materials availability
  - Data and code availability
- EXPERIMENTAL MODEL AND STUDY PARTICIPANT DETAILS
  - Animals and ethical statement
- METHOD DETAILS
  - Animals
  - Serum biochemistry
  - Echocardiography

- Histopathological examination
- Electron microscopy
- Immunofluorescence staining
- Sample preparation for snRNA-seq
- SnRNA-seq analysis
- Data quality control, filtering and clustering
- Differentially expressed genes analysis
- Pathway enrichment analysis
- Cell-cell interactions
- Bulk RNA sequencing and analysis

- QUANTIFICATION AND STATISTICAL ANALYSIS

SUPPLEMENTAL INFORMATION

Supplemental information can be found online at https://doi.org/10.1016/j.isci.2024.110015.

ACKNOWLEDGMENTS

We acknowledge Dr. Yong Li of BGI Institute of Applied Agriculture (Shenzhen, China) for assistance in animal breeding. We thank Dr. Guangxin Yue, Dr.Hong Lian, and Dr. Jubo Li of State Key Laboratory of Cardiovascular Diseases, Fuwai Hospital, National Center for Cardiovascular Diseases, Chinese Academy of Medical Sciences (Beijing, China) for support in cardiac Imaging. We acknowledge Gene Denovo Biotechnology Co., Ltd (Guangzhou, China) for support with sample processing and sequencing. Research was funded by The National Key R&D Program of China (2021YFA0805903), The National Natural Science Foundation of China (grant no. 32070535), and The Agricultural Science and Technology Innovation Program (grant no. ASTIP-IAS05).

AUTHOR CONTRIBUTIONS

J.M. performed the experiments, data analyses and wrote the manuscript. J.M., K.Z., Y.Y., S.X., and J.D. facilitated sample collection and performed the experiments. C.T. and T.W. participated in the construction of transgenic animals. Y.W. and S.Y. provided conceptual insights and edited the manuscript. All authors contributed to the article and approved the final manuscript.

DECLARATION OF INTERESTS

The authors declare no competing interests.

Received: December 11, 2023
Revised: March 28, 2024
Accepted: May 14, 2024
Published: May 16, 2024

REFERENCES

1. Esser, N., Paquot, N., and Scheen, A.J. (2015). Anti-inflammatory agents to treat or prevent type 2 diabetes, metabolic syndrome and cardiovascular disease. Expert Opin. Investig. Drugs *24*, 283–307. https://doi.org/10.1517/13543784.2015.974804.
2. Goswami, S.K., Ranjan, P., Dutta, R.K., and Verma, S.K. (2021). Management of inflammation in cardiovascular diseases. Pharmacol. Res. *173*, 105912. https://doi.org/10.1016/j.phrs.2021.105912.
3. Kosmala, W., Sanders, P., and Marwick, T.H. (2017). Subclinical Myocardial Impairment in Metabolic Diseases. JACC. Cardiovasc. Imaging *10*, 692–703. https://doi.org/10.1016/j.jcmg.2017.04.001.
4. Litvinukova, M., Talavera-Lopez, C., Maatz, H., Reichart, D., Worth, C.L., Lindberg, E.L., Kanda, M., Polanski, K., Heinig, M., Lee, M., et al. (2020). Cells of the adult human heart. Nature *588*, 466–472. https://doi.org/10.1038/s41586-020-2797-4.
5. McLellan, M.A., Skelly, D.A., Dona, M.S.I., Squiers, G.T., Farrugia, G.E., Gaynor, T.L., Cohen, C.D., Pandey, R., Diep, H., Vinh, A., et al. (2020). High-Resolution Transcriptomic Profiling of the Heart During Chronic Stress Reveals Cellular Drivers of Cardiac Fibrosis and Hypertrophy. Circulation *142*, 1448–1463. https://doi.org/10.1161/CIRCULATIONAHA.119.045115.
6. Cui, Y., Zheng, Y., Liu, X., Yan, L., Fan, X., Yong, J., Hu, Y., Dong, J., Li, Q., Wu, X., et al. (2019). Single-Cell Transcriptome Analysis Maps the Developmental Track of the Human Heart. Cell Rep. *26*, 1934–1950.e5. https://doi.org/10.1016/j.celrep.2019.01.079.
7. Koenig, A.L., Shchukina, I., Amrute, J., Andhey, P.S., Zaitsev, K., Lai, L., Bajpai, G., Bredemeyer, A., Smith, G., Jones, C., et al. (2022). Single-cell transcriptomics reveals cell-type-specific diversification in human heart failure. Nat. Cardiovasc. Res. *1*, 263–280. https://doi.org/10.1038/s44161-022-00028-6.
8. Li, G., Xu, A., Sim, S., Priest, J.R., Tian, X., Khan, T., Quertermous, T., Zhou, B., Tsao, P.S., Quake, S.R., and Wu, S.M. (2016). Transcriptomic Profiling Maps Anatomically Patterned Subpopulations among Single Embryonic Cardiac Cells. Dev. Cell *39*, 491–507. https://doi.org/10.1016/j.devcel.2016.10.014.
9. Wang, L., Yu, P., Zhou, B., Song, J., Li, Z., Zhang, M., Guo, G., Wang, Y., Chen, X., Han, L., and Hu, S. (2020). Single-cell reconstruction of the adult human heart during heart failure and recovery reveals the cellular landscape underlying cardiac function. Nat. Cell Biol. *22*, 108–119. https://doi.org/10.1038/s41556-019-0446-7.
10. Rao, M., Wang, X., Guo, G., Wang, L., Chen, S., Yin, P., Chen, K., Chen, L., Zhang, Z., Chen, X., et al. (2021). Resolving the intertwining of inflammation and fibrosis in human heart failure at single-cell level. Basic Res. Cardiol. *116*, 55. https://doi.org/10.1007/s00395-021-00897-1.
11. Chaffin, M., Papangeli, I., Simonson, B., Akkad, A.D., Hill, M.C., Arduini, A., Fleming, S.J., Melanson, M., Hayat, S., Kost-Alimova, M., et al. (2022). Single-nucleus profiling of human dilated and hypertrophic cardiomyopathy. Nature *608*, 174–180. https://doi.org/10.1038/s41586-022-04817-8.

12. Gabriel, G.C., Devine, W., Redel, B.K., Whitworth, K.M., Samuel, M., Spate, L.D., Cecil, R.F., Prather, R.S., Wu, Y., Wells, K.D., and Lo, C.W. (2021). Cardiovascular Development and Congenital Heart Disease Modeling in the Pig. J. Am. Heart Assoc. *10*, e021631. https://doi.org/10.1161/JAHA.121.021631.
13. Zhang, K., Tao, C., Xu, J., Ruan, J., Xia, J., Zhu, W., Xin, L., Ye, H., Xie, N., Xia, B., et al. (2021). CD8(+) T Cells Involved in Metabolic Inflammation in Visceral Adipose Tissue and Liver of Transgenic Pigs. Front. Immunol. *12*, 690069. https://doi.org/10.3389/fimmu.2021.690069.
14. Voulgari, C., Moyssakis, I., Papazafiropoulou, A., Perrea, D., Kyriaki, D., Katsilambros, N., and Tentolouris, N. (2010). The impact of metabolic syndrome on left ventricular myocardial performance. Diabetes. Metab. Res. Rev. *26*, 121–127. https://doi.org/10.1002/dmrr.1063.
15. Simonson, B., Chaffin, M., Hill, M.C., Atwa, O., Guedira, Y., Bhasin, H., Hall, A.W., Hayat, S., Baumgart, S., Bedi, K.C., Jr., et al. (2023). Single-nucleus RNA sequencing in ischemic cardiomyopathy reveals common transcriptional profile underlying end-stage heart failure. Cell Rep. *42*, 112086. https://doi.org/10.1016/j.celrep.2023.112086.
16. Ren, Z., Yu, P., Li, D., Li, Z., Liao, Y., Wang, Y., Zhou, B., and Wang, L. (2020). Single-Cell Reconstruction of Progression Trajectory Reveals Intervention Principles in Pathological Cardiac Hypertrophy. Circulation *141*, 1704–1719. https://doi.org/10.1161/CIRCULATIONAHA.119.043053.
17. Kalucka, J., de Rooij, L.P.M.H., Goveia, J., Rohlenova, K., Dumas, S.J., Meta, E., Conchinha, N.V., Taverna, F., Teuwen, L.A., Veys, K., et al. (2020). Single-Cell Transcriptome Atlas of Murine Endothelial Cells. Cell *180*, 764–779.e20. https://doi.org/10.1016/j.cell.2020.01.015.
18. Zhu, R., and Chen, S. (2023). Proteomic analysis reveals semaglutide impacts lipogenic protein expression in epididymal adipose tissue of obese mice. Front. Endocrinol. *14*, 1095432. https://doi.org/10.3389/fendo.2023.1095432.
19. Ren, R., Ding, S., Ma, K., Jiang, Y., Wang, Y., Chen, J., Wang, Y., Kou, Y., Fan, X., Zhu, X., et al. (2024). SUMOylation Fine-Tunes Endothelial HEY1 in the Regulation of Angiogenesis. Circ. Res. *134*, 203–222. https://doi.org/10.1161/CIRCRESAHA.123.323398.
20. Takahashi, T., Huynh-Do, U., and Daniel, T.O. (1998). Renal microvascular assembly and repair: power and promise of molecular definition. Kidney Int. *53*, 826–835. https://doi.org/10.1111/j.1523-1755.1998.00822.x.
21. Hsieh, M., Huang, P.J., Chou, P.Y., Wang, S.W., Lu, H.C., Su, W.W., Chung, Y.C., and Wu, M.H. (2022). Carbonic Anhydrase VIII (CAVIII) Gene Mediated Colorectal Cancer Growth and Angiogenesis through Mediated miRNA 16-5p. Biomedicines *10*, 1030. https://doi.org/10.3390/biomedicines10051030.
22. Domingues, A., Jolibois, J., Marquet de Rougé, P., and Nivet-Antoine, V. (2021). The Emerging Role of TXNIP in Ischemic and Cardiovascular Diseases; A Novel Marker and Therapeutic Target. Int. J. Mol. Sci. *22*, 169. https://doi.org/10.3390/ijms22041693.
23. Ling, S.S.M., Chen, Y.-T., Wang, J., Richards, A.M., and Liew, O.W. (2017). Ankyrin Repeat Domain 1 Protein: A Functionally Pleiotropic Protein with Cardiac Biomarker Potential. Int. J. Mol. Sci. *18*, 1362. https://doi.org/10.3390/ijms18071362.
24. Fan, G.-C., and Kranias, E.G. (2011). Small heat shock protein 20 (HspB6) in cardiac hypertrophy and failure. J. Mol. Cell. Cardiol. *51*, 574–577. https://doi.org/10.1016/j.yjmcc.2010.09.013.
25. Wu, Y.W., Chang, T.T., Chang, C.C., and Chen, J.W. (2020). Fatty-Acid-Binding Protein 4 as a Novel Contributor to Mononuclear Cell Activation and Endothelial Cell Dysfunction in Atherosclerosis. Int. J. Mol. Sci. *21*, 9245. https://doi.org/10.3390/ijms21239245.
26. Zhang, Q.-Y., Ye, X.-P., Zhou, Z., Zhu, C.-F., Li, R., Fang, Y., Zhang, R.-J., Li, L., Liu, W., Wang, Z., et al. (2022). Lymphocyte infiltration and thyrocyte destruction are driven by stromal and immune cell components in Hashimoto's thyroiditis. Nat. Commun. *13*, 775. https://doi.org/10.1038/s41467-022-28120-2.
27. Aird, W.C. (2007). Phenotypic heterogeneity of the endothelium: II. Representative vascular beds. Circ. Res. *100*, 174–190.
28. Martin, J.C., Chang, C., Boschetti, G., Ungaro, R., Giri, M., Grout, J.A., Gettler, K., Chuang, L.S., Nayar, S., Greenstein, A.J., et al. (2019). Single-Cell Analysis of Crohn's Disease Lesions Identifies a Pathogenic Cellular Module Associated with Resistance to Anti-TNF Therapy. Cell *178*, 1493–1508.e20. https://doi.org/10.1016/j.cell.2019.08.008.
29. Paulus, W.J., and Tschöpe, C. (2013). A novel paradigm for heart failure with preserved ejection fraction: comorbidities drive myocardial dysfunction and remodeling through coronary microvascular endothelial inflammation. J. Am. Coll. Cardiol. *62*, 263–271. https://doi.org/10.1016/j.jacc.2013.02.092.
30. Dick, S.A., Macklin, J.A., Nejat, S., Momen, A., Clemente-Casares, X., Althagafi, M.G., Chen, J., Kantores, C., Hosseinzadeh, S., Aronoff, L., et al. (2019). Self-renewing resident cardiac macrophages limit adverse remodeling following myocardial infarction. Nat. Immunol. *20*, 29–39. https://doi.org/10.1038/s41590-018-0272-2.
31. Zaman, R., and Epelman, S. (2022). Resident cardiac macrophages: Heterogeneity and function in health and disease. Immunity *55*, 1549–1563. https://doi.org/10.1016/j.immuni.2022.08.009.
32. Frangogiannis, N.G. (2021). Cardiac fibrosis. Cardiovasc. Res. *117*, 1450–1488. https://doi.org/10.1093/cvr/cvaa324.
33. Guo, M., Bao, E.L., Wagner, M., Whitsett, J.A., and Xu, Y. (2017). SLICE: determining cell differentiation and lineage based on single cell entropy. Nucleic Acids Res. *45*, e54. https://doi.org/10.1093/nar/gkw1278.
34. Wolf, F.A., Hamey, F.K., Plass, M., Solana, J., Dahlin, J.S., Göttgens, B., Rajewsky, N., Simon, L., and Theis, F.J. (2019). PAGA: graph abstraction reconciles clustering with trajectory inference through a topology preserving map of single cells. Genome Biol. *20*, 59. https://doi.org/10.1186/s13059-019-1663-x.
35. MacArthur, B.D., and Lemischka, I.R. (2013). Statistical mechanics of pluripotency. Cell *154*, 484–489. https://doi.org/10.1016/j.cell.2013.07.024.
36. Skelly, D.A., Squiers, G.T., McLellan, M.A., Bolisetty, M.T., Robson, P., Rosenthal, N.A., and Pinto, A.R. (2018). Single-Cell Transcriptional Profiling Reveals Cellular Diversity and Intercommunication in the Mouse Heart. Cell Rep. *22*, 600–610. https://doi.org/10.1016/j.celrep.2017.12.072.
37. Zaman, R., Hamidzada, H., Kantores, C., Wong, A., Dick, S.A., Wang, Y., Momen, A., Aronoff, L., Lin, J., Razani, B., et al. (2021). Selective loss of resident macrophage-derived insulin-like growth factor-1 abolishes adaptive cardiac growth to stress. Immunity *54*, 2057–2071.e6. https://doi.org/10.1016/j.immuni.2021.07.006.
38. Vago, J.P., Amaral, F.A., and van de Loo, F.A.J. (2021). Resolving inflammation by TAM receptor activation. Pharmacol. Ther. *227*, 107893. https://doi.org/10.1016/j.pharmthera.2021.107893.
39. Wienke, J., Pachman, L.M., Morgan, G.A., Yeo, J.G., Amoruso, M.C., Hans, V., Kamphuis, S.S.M., Hoppenreijs, E.P.A.H., Armbrust, W., van den Berg, J.M., et al. (2020). Endothelial and Inflammation Biomarker Profiles at Diagnosis Reflecting Clinical Heterogeneity and Serving as a Prognostic Tool for Treatment Response in Two Independent Cohorts of Patients With Juvenile Dermatomyositis. Arthritis Rheumatol. *72*, 1214–1226. https://doi.org/10.1002/art.41236.
40. Tilstam, P.V., Qi, D., Leng, L., Young, L., and Bucala, R. (2017). MIF family cytokines in cardiovascular diseases and prospects for precision-based therapeutics. Expert Opin. Ther. Targets *21*, 671–683. https://doi.org/10.1080/14728222.2017.1336227.
41. Liu, S.Q., Tefft, B.J., Roberts, D.T., Zhang, L.Q., Ren, Y., Li, Y.C., Huang, Y., Zhang, D., Phillips, H.R., and Wu, Y.H. (2012). Cardioprotective proteins upregulated in the liver in response to experimental myocardial ischemia. Am. J. Physiol. Heart Circ. Physiol. *303*, H1446–H1458. https://doi.org/10.1152/ajpheart.00362.2012.
42. Jiang, Y., Han, Q., Zhao, H., and Zhang, J. (2021). Promotion of epithelial-mesenchymal transformation by hepatocellular carcinoma-educated macrophages through Wnt2b/beta-catenin/c-Myc signaling and reprogramming glycolysis. J. Exp. Clin. Cancer Res. *40*, 13. https://doi.org/10.1186/s13046-020-01808-3.
43. Cameron, A.J., Shaw, J.E., and Zimmet, P.Z. (2004). The metabolic syndrome: prevalence in worldwide populations. Endocrinol. Metab. Clin. North Am. *33*, 351–375. https://doi.org/10.1016/j.ecl.2004.03.005.
44. Yuan, F., Woollard, J.R., Jordan, K.L., Lerman, A., Lerman, L.O., and Eirin, A. (2018). Mitochondrial targeted peptides preserve mitochondrial organization and decrease reversible myocardial changes in early swine metabolic syndrome. Cardiovasc. Res. *114*, 431–442. https://doi.org/10.1093/cvr/cvx245.
45. Rowland, T.W. (2007). Effect of obesity on cardiac function in children and adolescents: a review. J. Sports Sci. Med. *6*, 319–326.
46. Wu, L., Li, Y.F., Shen, J.W., Zhu, Q., Jiang, J., Ma, S.H., He, K., Ning, Z.P., Li, J., and Li, X.M. (2022). Single-cell RNA sequencing of mouse left ventricle reveals cellular diversity and intercommunication. Physiol. Genomics *54*, 11–21. https://doi.org/10.1152/physiolgenomics.00016.2021.
47. Hausenloy, D.J., and Yellon, D.M. (2013). Myocardial ischemia-reperfusion injury: a neglected therapeutic target. J. Clin. Invest. *123*, 92–100. https://doi.org/10.1172/JCI62874.
48. Swirski, F.K., and Nahrendorf, M. (2013). Leukocyte behavior in atherosclerosis, myocardial infarction, and heart failure.

Science *339*, 161–166. https://doi.org/10.1126/science.1230719.

49. Aird, W.C. (2007). Phenotypic heterogeneity of the endothelium: II. Representative vascular beds. Circ. Res. *100*, 174–190. https://doi.org/10.1161/01.RES.0000255690.03436.ae.
50. Balamurugan, K., Sharan, S., Klarmann, K.D., Zhang, Y., Coppola, V., Summers, G.H., Roger, T., Morrison, D.K., Keller, J.R., and Sterneck, E. (2013). FBXW7alpha attenuates inflammatory signalling by downregulating C/EBPdelta and its target gene Tlr4. Nat. Commun. *4*, 1662. https://doi.org/10.1038/ncomms2677.
51. Wang, X.Q., Nigro, P., World, C., Fujiwara, K., Yan, C., and Berk, B.C. (2012). Thioredoxin interacting protein promotes endothelial cell inflammation in response to disturbed flow by increasing leukocyte adhesion and repressing Kruppel-like factor 2. Circ. Res. *110*, 560–568. https://doi.org/10.1161/CIRCRESAHA.111.256362.
52. Yamawaki, H., Pan, S., Lee, R.T., and Berk, B.C. (2005). Fluid shear stress inhibits vascular inflammation by decreasing thioredoxin-interacting protein in endothelial cells. J. Clin. Invest. *115*, 733–738. https://doi.org/10.1172/JCI23001.
53. Manning, B.S., Shotwell, K., Mao, L., Rockman, H.A., and Koch, W.J. (2000). Physiological induction of a beta-adrenergic receptor kinase inhibitor transgene preserves ss-adrenergic responsiveness in pressure-overload cardiac hypertrophy. Circulation *102*, 2751–2757. https://doi.org/10.1161/01.cir.102.22.2751.
54. Bajpai, G., Schneider, C., Wong, N., Bredemeyer, A., Hulsmans, M., Nahrendorf, M., Epelman, S., Kreisel, D., Liu, Y., Itoh, A., et al. (2018). The human heart contains distinct macrophage subsets with divergent origins and functions. Nat. Med. *24*, 1234–1245. https://doi.org/10.1038/s41591-018-0059-x.
55. Leid, J., Carrelha, J., Boukarabila, H., Epelman, S., Jacobsen, S.E.W., and Lavine, K.J. (2016). Primitive Embryonic Macrophages are Required for Coronary Development and Maturation. Circ. Res. *118*, 1498–1511. https://doi.org/10.1161/CIRCRESAHA.115.308270.
56. Dick, S.A., Wong, A., Hamidzada, H., Nejat, S., Nechanitzky, R., Vohra, S., Mueller, B., Zaman, R., Kantores, C., Aronoff, L., et al. (2022). Three tissue resident macrophage subsets coexist across organs with conserved origins and life cycles. Sci. Immunol. *7*, eabf7777. https://doi.org/10.1126/sciimmunol.abf7777.
57. Chakarov, S., Lim, H.Y., Tan, L., Lim, S.Y., See, P., Lum, J., Zhang, X.M., Foo, S., Nakamizo, S., Duan, K., et al. (2019). Two distinct interstitial macrophage populations coexist across tissues in specific subtissular niches. Science *363*, eaau0964. https://doi.org/10.1126/science.aau0964.
58. Lim, H.Y., Lim, S.Y., Tan, C.K., Thiam, C.H., Goh, C.C., Carbajo, D., Chew, S.H.S., See, P., Chakarov, S., Wang, X.N., et al. (2018). Hyaluronan Receptor LYVE-1-Expressing Macrophages Maintain Arterial Tone through Hyaluronan-Mediated Regulation of Smooth Muscle Cell Collagen. Immunity *49*, 326–341.e7. https://doi.org/10.1016/j.immuni.2018.06.008.
59. Hulsmans, M., Clauss, S., Xiao, L., Aguirre, A.D., King, K.R., Hanley, A., Hucker, W.J., Wülfers, E.M., Seemann, G., Courties, G., et al. (2017). Macrophages Facilitate Electrical Conduction in the Heart. Cell *169*, 510–522.e20. https://doi.org/10.1016/j.cell.2017.03.050.
60. Hu, S., Yang, M., Huang, S., Zhong, S., Zhang, Q., Ding, H., Xiong, X., Hu, Z., and Yang, Y. (2022). Different Roles of Resident and Non-resident Macrophages in Cardiac Fibrosis. Front. Cardiovasc. Med. *9*, 818188. https://doi.org/10.3389/fcvm.2022.818188.
61. Bajpai, G., Bredemeyer, A., Li, W., Zaitsev, K., Koenig, A.L., Lokshina, I., Mohan, J., Ivey, B., Hsiao, H.M., Weinheimer, C., et al. (2019). Tissue Resident CCR2- and CCR2+ Cardiac Macrophages Differentially Orchestrate Monocyte Recruitment and Fate Specification Following Myocardial Injury. Circ. Res. *124*, 263–278. https://doi.org/10.1161/CIRCRESAHA.118.314028.
62. Lavine, K.J., Epelman, S., Uchida, K., Weber, K.J., Nichols, C.G., Schilling, J.D., Ornitz, D.M., Randolph, G.J., and Mann, D.L. (2014). Distinct macrophage lineages contribute to disparate patterns of cardiac recovery and remodeling in the neonatal and adult heart. Proc. Natl. Acad. Sci. USA *111*, 16029–16034. https://doi.org/10.1073/pnas.1406508111.
63. Aurora, A.B., Porrello, E.R., Tan, W., Mahmoud, A.I., Hill, J.A., Bassel-Duby, R., Sadek, H.A., and Olson, E.N. (2014). Macrophages are required for neonatal heart regeneration. J. Clin. Invest. *124*, 1382–1392. https://doi.org/10.1172/JCI72181.
64. Schneider, C.A., Rasband, W.S., and Eliceiri, K.W. (2012). NIH Image to ImageJ: 25 years of image analysis. Nat. Methods *9*, 671–675.
65. Love, M.I., Huber, W., and Anders, S. (2014). Moderated estimation of fold change and dispersion for RNA-seq data with DESeq2. Genome Biol. *15*, 550.
66. Satija, R., Farrell, J.A., Gennert, D., Schier, A.F., and Regev, A. (2015). Spatial reconstruction of single-cell gene expression data. Nat. Biotechnol. *33*, 495–502. https://doi.org/10.1038/nbt.3192.
67. Ruan, J., Li, H., Xu, K., Wu, T., Wei, J., Zhou, R., Liu, Z., Mu, Y., Yang, S., Ouyang, H., et al. (2015). Highly efficient CRISPR/Cas9-mediated transgene knockin at the H11 locus in pigs. Sci. Rep. *5*, 14253. https://doi.org/10.1038/srep14253.
68. Yang, S.L., Xia, J.H., Zhang, Y.Y., Fan, J.G., Wang, H., Yuan, J., Zhao, Z.Z., Pan, Q., Mu, Y.L., Xin, L.L., et al. (2015). Hyperinsulinemia shifted energy supply from glucose to ketone bodies in early nonalcoholic steatohepatitis from high-fat high-sucrose diet induced Bama minipigs. Sci. Rep. *5*, 13980. https://doi.org/10.1038/srep13980.

STAR★METHODS

KEY RESOURCES TABLE

REAGENT or RESOURCE	SOURCE	IDENTIFIER
Antibodies		
Anti-Cardiac Troponin T antibody	Abcam	Cat# ab8295; RRID: AB_306445
Anti-CD31 antibody	Abcam	Cat# ab28364; RRID: AB_726362
Anti-CD163 antibody	Abcam	Cat# ab156769; RRID: AB_3076143
Donkey Anti-Mouse IgG H&L (Alexa Fluor® 488)	Abcam	Cat# ab150105; RRID: AB_2732856
Goat Anti-Rabbit IgG H&L (Alexa Fluor® 594)	Abcam	Cat# ab150080; RRID: AB_2650602
TPT1 Polyclonal antibody	Proteintech	Cat# 10824-1-AP; RRID: AB_2287617
LYVE1 Monoclonal Antibody	Thermo fisher	Cat# 14-0443-82; RRID: AB_1633414
VCAM-1 Monoclonal Antibody	Thermo fisher	Cat# MA5-11447; RRID: AB_10979792
Critical commercial assays		
Nonesterified Free fatty acids assay kit	NJJCBIO	Cat# A042-2-1
Porcine Insulin ELISA	Mercodia	Cat# 10-1200-01
Glucagon ELISA	Mercodia	Cat# 10-1281-01
Porcine C-Reactive Protein DuoSet ELISA	R&D Systems	Cat# DY2648
Human Leptin Quantikine ELISA Kit	R&D Systems	Cat# DLP00
Human Total Adiponectin Quantikine ELISA	R&D Systems	Cat# DRP300
Chromium Next GEM Single Cell 3′ Reagent Kits v3.1	10× Genomics	Cat# 1000075
RNA-pure Total RNA Fast Isolation Kit	BioTeke	Cat# RP1202
Deposited data		
Raw snRNA-seq data	This paper	Gene Expression Omnibus (GEO): GSE245458
Raw bulk RNA-seq data	This paper	Sequence Read Archive (SRA): PRJNA1048872
Experimental models: Organisms/strains		
Pig: Bama Miniature Pig	Institute of Animal Sciences, Chinese Academy of Agricultural Sciences	N/A
Pig: PNPLA3^{I148M}-GIPR^{dn}-HIAPP pig	This paper	N/A
Software and algorithms		
(Fuji is just) ImageJ	Schneider et al.[64]	https://imagej.nih.gov
DESeq2 v1.20.0	Love et al.[65]	https://doi.org/10.18129/B9.bioc.DESeq2
Custom snRNA-seq analysis code	This paper	https://github.com/apanhui/scRNA_analysis
R v3.5.1	R Foundation	https://www.r-project.org/
Cell Ranger v3.1.0	10x Genomics	https://support.10xgenomics.com/single-cell-vdj/software/overview/welcome
Seurat v3.1.1	Satija et al.[66]	https://github.com/satijalab/seurat

RESOURCE AVAILABILITY

Lead contact

Further information and requests for resources and reagents should be directed to and will be fulfilled by the lead contact, Shulin Yang (yangshulin@caas.cn).

Materials availability

The triple-transgenic pig model (*PNPLA3^{I148M}-GIPR^{dn}-hIAPP*) constructed in this study is maintained at the Institute of Animal Sciences, Chinese Academy of Agricultural Sciences. All biological samples are available on a reasonable request from the lead contact, Shulin Yang (yangshulin@caas.cn).

Data and code availability

- SnRNA-seq data associated with this study have been deposited in the Gene Expression Omnibus (GEO) (https://www.ncbi.nlm.nih.gov/geo/) under accession number GSE245458, and bulk RNA-seq data have been deposited in the Sequence Read Archive (SRA) (https://trace.ncbi.nlm.nih.gov/Traces/sra/) under accession number PRJNA1048872, and these accession numbers are also listed in the key resources table. All datasets in this study are publicly available. Microscopy data reported in this paper will be shared by the lead contact upon request.
- All original code has been deposited at GitHub: https://github.com/apanhui/scRNA_analysis and is publicly available. Any additional analysis was performed using publicly available programs and analytical packages as outlined in the key resources table.
- Any additional information required to reanalyze the data reported in this paper is available from the lead contact upon request.

EXPERIMENTAL MODEL AND STUDY PARTICIPANT DETAILS

Animals and ethical statement

All animal experiments were performed in accordance with the "Guide for the Care and Use of Laboratory Animals, ISA, CAAS", the protocol was approved by the Animal Care and Use Committee of the Germplasm Resource Center of Chinese Experimental Minipigs (Institute of Animal Sciences, Chinese Academy of Agricultural Sciences, permit No. IAS2019-12). Male Bama Minipigs (both wild-type and transgenic) at 6 months of age were used in this study and fed until 18 months of age. During the experimental period, pigs were housed in single pens, and the ambient temperature was 20°C–26°C, the humidity was 40–70%, and the light cycle was 12 h day/12 h night.

METHOD DETAILS

Animals

The details of genetically modified Bama Pigs construction could be found in our previous studies.[13,67] Briefly, using the plasmid vector of CRISPR/Cas9 system targeting pig H11 locus that has been constructed in our laboratory before, three risk genes (*PNPLA3*^{I148M}-*GIPR*^{dn}-*hIAPP*) were targeted knock-in Bama pigs, among which human *PNPLA3*^{I148M} (NM_025225.3, rs738409, C > G) was specifically expressed in liver, while *GIPR*^{dn} and *hIAPP* (NM_000415.2) were specifically expressed in the pancreas. A total of 4 triple-transgenic males (F_3 generation) and 4 wild-type males were used in this experiment, which were matched in age and initial body weight. All the pigs were fed with a control diet until 6 months, and after 6 months, fed a high-fat and high-sucrose diet (HFHSD, containing 37% sucrose, 53% control diet and 10% pork lard) twice daily.[68]

After 12 months of HFHSD intervention, animal serum was collected for metabolic parameters detection, and echocardiography was performed to evaluate cardiac morphology and function. After that, animals were euthanized and cardiac tissue was collected for histopathological analysis and snRNA-seq.

Serum biochemistry

After overnight fasting, blood samples (20 mL) were collected from the anterior vena cava of pigs into vacutainer tubes (KJ030AS, Kangjian), and allowed to clot at room temperature for 60 min. Serum was separated from whole blood by centrifugation at 3,000 rpm for 10 min at 4°C. Serum concentrations of total cholesterol (TC), triglyceride (TG), low-density lipoprotein cholesterol (LDL-C), high-density lipoprotein cholesterol (HDL-C), glucose (GLU), creatine kinase (CK), creatine kinase-MB (CK-MB), lactate dehydrogenase (LDH), aspartate aminotransferase (AST) and creatinine (CREA) were measured by AU480 automatic analyzer (Olympus Corporation). Non-esterified fatty acids (NEFA) were measured by an enzymatic assay kit (A042-2-1, NJJCBIO). Insulin (10-1200-01, Mercodia), Glucagon (10-1281-01, Mercodia), C-reactive protein (CRP) (DY2648, R&D), Leptin (DLP00, R&D) and adiponectin were measured using ELISA prime (DRP300, R&D) levels.

Echocardiography

The ultrasound diagnostic imaging system equipped with a Cardiac PA122 phased array transducer (MyLab30, Esatoe, Italy) was used to evaluate cardiac morphology and function after 12 months of HFHSD intervention. After anesthetized with ketamine hydrochloride, a transducer was placed in the right intercostal area to obtain B-mode and M-mode images of the left ventricular long axis. M-mode echocardiographic measurements included the left ventricular dimensions at the end of systole and diastole (LVEDs and LVEDd), and the posterior wall thickness at the end of systole and diastole (LVPWs and LVPWd). The software provided by Esaote Inc. was used to analyze left ventricular ejection fraction (EF) and fractional shortening (FS).

Histopathological examination

HE staining was used to examine the morphology and damage of cardiac tissue. Pigs were euthanized with pentobarbital sodium at the end of the experiment and then collected left ventricle, interventricular septum, and aortic vessel tissue. Tissue blocks were then fixed overnight in 4% paraformaldehyde. The fixed tissue was embedded in paraffin and cut into 4 μm-thick continuous sections. Panoramic scanning and reading of tissue sections by NanoZoomer digital slide scanner (C13220-01, Hamamatsu, Japan).

Electron microscopy

Tissue obtained from the left ventricle was immediately pre-fixed with 2.5% glutaraldehyde and stored at 4°C. Post-fixation with 1% osmium tetroxide followed by an increasing gradient dehydration step using ethanol and propylene oxide. Sections were sectioned ultrathin (90 nm) (EM-UC7, Leica, Germany) onto uncoated copper grids, and stained with 0.2% lead citrate and 1% uranyl acetate. Images were examined using a transmission electron microscope (H-7500, Hitachi, Japan) to obtain high-power photomicrographs (×15,000–30,000) from multiple different low-power fields in each myocardial sample.

Immunofluorescence staining

Immunofluorescence staining was performed on left ventricle following the standard protocols for paraffin-embedded samples. Briefly, embedded left ventricular myocardium samples were sectioned at a thickness of 4 μm and subsequently de-paraffinized according to the xylene-ethanol gradient protocol. Antigen retrieval was performed using EDTA buffer (pH 9.0) at 95°C. Sections were then blocked in 5% BSA solution for 1 h. Antibodies used were as follows: anti-TNNT2 (Abcam, ab8295) at 1:500, anti-TPT1 (Proteintech, 10824-1-AP) at 1:100, anti-PECAM1 (Abcam, ab28364) at 1:50, anti-VCAM1 (Thermo fisher, MA5-11447) at 1:50, anti-CD163 (Abcam, ab156769) at 1:100 and anti-LYVE1 (Thermo fisher, 14-0443-82) at 1:200. Alexa Flour 488 donkey anti-mouse IgG and Alex Fluor 594 goat anti-rabbit IgG secondary antibodies (Abcam, ab150105, ab150080) were used for fluorescent labeling. Sections incubated with secondary antibodies only were used as negative controls. Images were taken using a laser-scanning confocal microscope (TCS-SP8, Leica, Germany) and processed using ImageJ software.[64]

Sample preparation for snRNA-seq

To prepare snRNA-seq samples, we randomly selected an animal from triple-transgenic group (TG) and wild-type group (WT), respectively. Frozen heart tissue from the left ventricular free wall was minced with a blade and transferred to a Dounce homogenizer containing 500 μL of chilled lysis buffer. Samples were gently homogenized five to ten times without rotation, then incubated on ice for 5 min. A 700 μL lysis buffer was added to the lysate and filtered gently through a 70 μm filter into a 50 mL centrifuge tube. Then 1 mL 50% of iodixanol was added to the filtrate and mixed gently. A total of 2 mL of the nuclei suspension was transferred into a 15 mL centrifuge tube containing 3 mL of chilled iodixanol gradient solution (1 mL 33% iodixanol, 2 mL 30% iodixanol). Nuclei were recovered after centrifugation and resuspended gently in wash buffer, followed by counting on a hemocytometer.

SnRNA-seq analysis

Nuclei were processed with the Chromium Next GEM Single Cell 3′ Reagent Kits v3.1 from 10× Genomics. In brief, cellular suspensions were loaded on a 10× Genomics GemCode Single-cell instrument to generate single-cell Gel Bead-In-EMlusion (GEMs). After the dissolution of the Gel Bead in a GEM, reverse transcription, barcoding, complementary DNA amplification and purification for sequencing libraries preparation was performed according to the Single Cell 3′ protocol.

Data quality control, filtering and clustering

Reads were mapped to the Sscrofa11.1 reference genome (Ensembl release104, http://asia.ensembl.org) using the 10× Genomics Cell Ranger software (version 3.1.0) with default parameters. After mapping, UMI sequences were corrected for sequencing errors, with empty droplets removed according to the EmptyDrops method. The cell by gene matrices were produced via UMI counting and cell barcodes calling. The cell by gene matrices for each sample were individually imported to Seurat (version 3.1.1)[66] for downstream analysis. Cells with the following criteria were filtered out: (1) unusually high number of UMIs (≥24000), (2) percentage of mitochondrial genes ≥25%, (3) genes fewer than 200 or more than 5100, (4) doublet GEMs. We utilized the DoubletFinder tool to filter doublet GEMs. Briefly, using DoubletFinder to generate artificial doublets, using the PC distance to find each cell's proportion of artificial k nearest neighbors (pANN) and ranking them according to the expected number of doublets. After removing unwanted cells from the dataset, we employed a global-scale normalization method "LogNormalize" to normalize the gene expression measurements of each cell to the total expression, and then perform log-transformation according to the formula: A gene expression level = $log\left(1 + \frac{UMI_A}{UMI_{Total}} \times 10000\right)$. Then data integration and batch effect correction were performed using the R package, Harmony. The Harmony algorithm inputs a PCA embedding of cells, along with their batch assignments, and returns a batch-corrected embedding. The integrated expression matrix is then scaled and principal component analysis (PCA) is performed for dimensionality reduction.

Cell clustering was performed using Seurat. Briefly, Seurat embed cells in a shared-nearest neighbor (SNN) graph, with edges drawn between cells via similar gene expression patterns. To partition this graph into highly interconnected quasi-cliques or communities, we first constructed the SNN graph based on the euclidean distance in PCA space and refined the edge weights between any two cells based on the shared overlap in their local neighborhoods (Jaccard distance). We then cluster cells using the Louvain method to maximize modularity.

Differentially expressed genes analysis

To help annotate the subpopulations of each cell type and dissect changes in cell subpopulations' transcriptional patterns in different states, we compared the expression value of each gene in a given cluster with the rest of the cells using the Wilcoxon rank-sum test to calculate differentially expressed genes (DEGs). DEGs should meet the following criteria: (1) at least 1.28-fold up- or down-expression in the target

cluster (2) expressed in more than 25% of cells belonging to the target cluster (3) *p* value less than 0.05 (unless stated otherwise in the analysis section).

Pathway enrichment analysis

Gene Ontology (GO) enrichment analysis and Kyoto Encyclopedia of Genes and Genomes (KEGG) pathway analysis were performed. As mentioned before, the list of DEGs calculated from Seurat differential expression analysis was used for pathway enrichment analysis. The calculated *p*-value was performed FDR Corrected, with a threshold of FDR $\leq$0.05. GO terms or KEGG pathways meeting this condition were defined as significantly enriched among DEGs.

Cell-cell interactions

The pig genes were transformed to corresponding human homologs using NCBI's HomoloGene database. CellphoneDB (version 2.0) was used to predict cell-cell interactions based on the log-normalized gene expression matrix. The parameters are set as follows: "iterations" to 1000, "threshold" to 0.1, and "*p*-value" to 0.05.

Bulk RNA sequencing and analysis

Bulk RNA sequencing (bulk RNA-seq) samples were collected from left ventricular free wall tissue from TG group (n = 3) and WT group (n = 3). Total RNA of myocardium samples was extracted using an RNA-pure Total RNA Fast Isolation Kit (BioTeke, China) according to the manufacturer's protocol, and subsequently quantified using a NanoDrop (Thermo Fisher, USA). RNA quality was assessed using a bioanalyzer (Agilent 2100, Agilent Technologies, USA) and all samples had RNA integrity values greater than 7.0. We used the NEBNext Ultra RNA Library Prep Kit (NEB#7530, New England Biolabs, USA) to reverse-transcribe the mRNA into cDNA, then added A bases and ligated with Illumina sequencing adapters. The resulting cDNA library was sequenced using Illumina Novaseq6000.

Clean reads filtered by fastp (version 0.18.0) were mapped to the same version of the reference genome (Sscrofa11.1) used for snRNA-seq data. We used RESM software to calculate the FPKM (fragment per kilobase of transcript per million mapped reads) value to quantify gene expression. Differential expression analysis between different groups was implemented using DESeq2 (version 1.20.0).[65] Genes with the parameter of *p* value below 0.05 and absolute fold change $\geq$1.28 were considered as differentially expressed genes (DEGs).

QUANTIFICATION AND STATISTICAL ANALYSIS

For snRNA-seq data, Wilcoxon rank-sum tests were used to detect differential genes. For all other data, an independent samples *t*-test (SPSS19) was used for statistical analyses. Data were displayed as means $\pm$ standard error of the mean (SEM). Significant differences at $p < 0.05$, 0.01 and 0.001 levels were indicated as *, ** and ***, respectively.